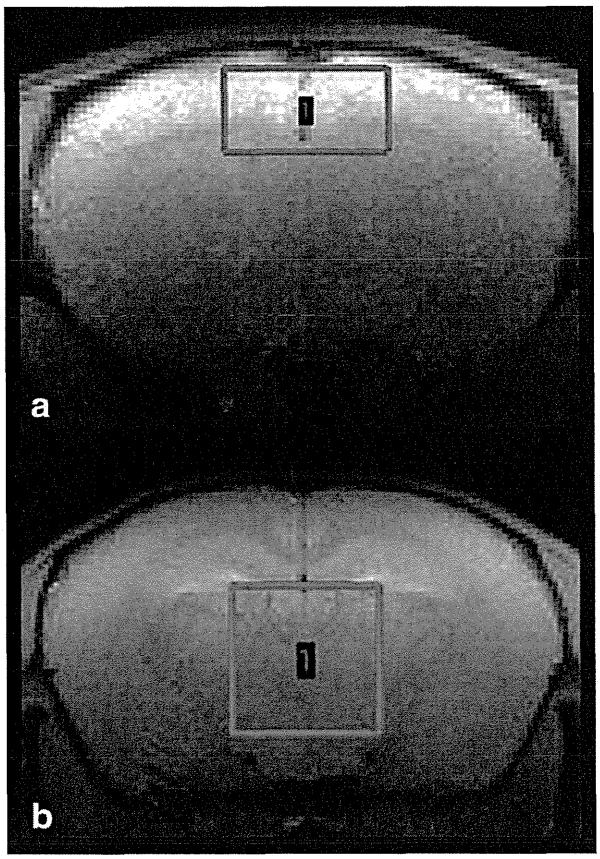

Figure 1. Coronal T1-weighted images show the ROI in the cortex (**a**) and thalamus (**b**) used for ^{1}H-MRS. [Color figure can be viewed in the online issue, which is available atwileyonlinelibrary.com.]

human PMD (7). Increased tNAA should attract attention because NAA is generally considered an important marker of neurons and axons (8,9), and is usually decreased in many neurodegenerative disorders. We performed ^{1}H-MRS in shiverer mice to determine the neurochemical changes associated with hypomyelination, especially to clarify whether or not increased tNAA with decreased Cho detectable on ^{1}H-MRS is a common finding for hypomyelinating disorders.

MATERIALS AND METHODS

Animals

The experimental animals included postnatal 12-week (12W) shiverer mice (*shi/shi*, maintained in the ICR background; $n=7$, 2 males and 5 females, weight = 32.5 ± 3.8 g), heterozygous mice (*shi/+*) ($n=8$, 3 males and 5 females, weight = 37.0 ± 6.1 g), and wild-type ICR mice ($n=8$, 4 males and 4 females, weight = 40.8 ± 7.3 g). Shiverer mice exhibit progressive tremors and tonic seizures early in life, which cause their premature death between 3 and 5 months of age. The animals had free access to food and water and were kept under standard laboratory conditions of 22–23°C room temperature, around 50% humidity, and a 12:12 hour light/dark cycle. Immediately prior to and during the MRI scanning, all mice were anesthetized with 2% isoflurane (Mylan Japan, Japan). The rectal temperature was continuously monitored and maintained at 36.5 ± 0.5°C using a heating pad throughout all experiments. During MRI scanning, the mice lay in the prone position on an MRI-compatible cradle and were held in place by a hand-made ear bar and anesthetized through a facemask with 2% isoflurane. The study protocols were approved by the Animal Welfare Committee of the National Institute of Radiological Sciences and that of the Ibaraki Prefectural University of Health Sciences.

MRI and ^{1}H-MRS Measurements

MRI and ^{1}H-MRS were performed on a 7.0T MRI scanner (20 cm bore, Biospec, Avance-III system; Bruker Biospin, Ettlingen, Germany) with a volume coil for transmission (86 mm i.d., Bruker Biospin) and a 2-channel phased-array cooled surface coil for reception (cryoprobe for mouse brain, Bruker Biospin), using almost the same methods as those previously reported (6). Briefly, coronal, sagittal, and axial multislice T1-weighted imaging (T1WI: multislice spin echo [SE]; repetition time [TR] / echo time [TE] = 400/9.57 msec) and coronal T2-mapping (multislice SE sequence, TR = 3000 msec, TE ranging from 20 to 100 msec in steps of 10 msec) were performed. T2 values were calculated in the white matter, thalamus, and cortex with image analysis software MRVision (MRVision, Winchester, MA). For single-voxel ^{1}H-MRS, a region of interest (ROI) was chosen predominantly in the

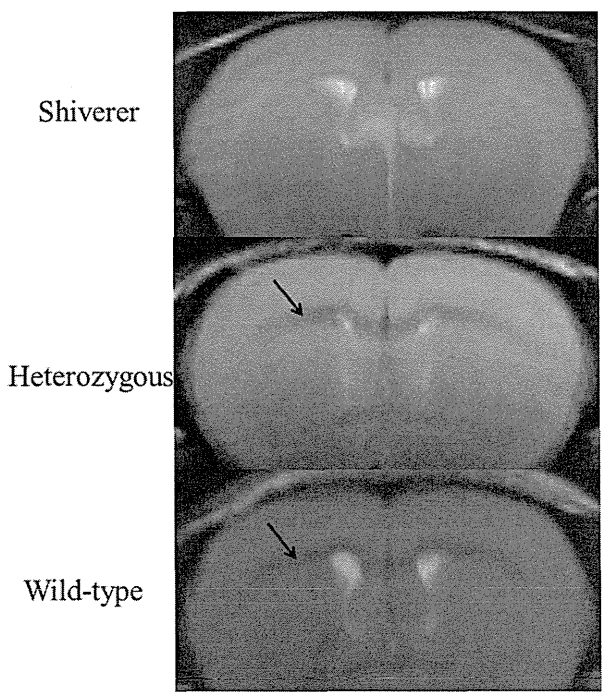

Figure 2. Coronal T2-weighted images (TE = 60 msec) of heterozygous and wild-type mice typically demonstrate a three-layered structure, ie, a low signal layer of white matter (arrows) between the cortex and caudate putamen, which was difficult to distinguish in shiverer mouse.

Table 1
T2 value of each region

	T2 value (msec, mean±SD)		
	Shiverer	Heterozygous	Wild-type
Cortex	53.3±1.8	52.3±2.0	53.1±3.3
Thalamus	53.8±1.9	51.8±2.3	51.4±2.3
White matter	55.8±1.3	48.2±1.4	48.0±1.2

***, p<0.001.

thalamus or cortex, with volumes of interest of 3.0 × 3.0 × 3.0 mm and 3.0 × 3.0 × 1.5 mm, respectively, as determined on T1WI (Fig. 1). Outer volume suppression combined with a point-resolved spectroscopy sequence was used for signal acquisition (number of repetitions = 192; TR = 4000 msec; TE = 20 msec; spectral bandwidth = 4 kHz; number of data points = 2048). ^{1}H-MRS was quantitatively analyzed using the modified water scaling method of LCModel, that is, the concentration was corrected by the T2 value of the ROI, as multiplied by R = exp (−20/T2_ROI)/0.7 (6,10). The concentrations of tNAA, creatine (Cr), Cho, myo-inositol (mIns), glutamine (Gln), and glutamate (Glu) were considered to show acceptable reliability when the LCModel showed percent of standard deviation (%SD) values of less than 20 (a smaller %SD is associated with more reliable data) (11,12).

Statistical Analysis of Metabolites

A two-way analysis of variance (ANOVA) was conducted, setting tNAA, Cr, Cho, mIns, Gln, and Glu as the dependent variables, the groups (shiverer, heterozygous, and wild-type), and the measurement sites (thalamus and cortex) as the independent variables. For each group in each measurement site, mean and SD were calculated, followed by Bonferroni's multiple comparison test on the mean difference, taking 0.05 as the significance level in testing statistical significance. The tool used for the analysis was IBM SPSS Statistics 20 (Armonk, NY).

Histological and Immunohistochemical Analyses

Two mice in each group, ie, shiverer, heterozygous, and wild-type mice, at 12W were subjected to Luxol Fast Blue (LFB) staining and immunohistochemical analysis. Coronal sections of 5 μm thickness of brain samples were prepared for these studies. The following primary antibodies were used: rat anti-Mbp antibody (1:1,000, Millipore, Bedford, MA; MAB395-IML), rabbit anti-Gfap antibody (1:500, Dako, Carpinteria, CA), rabbit anti-Olig 2 (1:100, IBL), and mouse anti-NeuN antibody (1:100, Millipore, MAB377). We defined degree of staining in the white matter, thalamus, and cortex: (−) as almost no staining, (+) as staining less than wild-type mice, (++) as staining similar to wild-type mice, (+++) as staining stronger than wild-type mice.

RESULTS

MRI Findings and T2 Value Measurement

Coronal T2 value mapping (TE = 60 msec of T2 mapping) of heterozygous and wild-type mice typically demonstrated a three-layered structure, ie, a low signal (shorter T2 value) layer of white matter between the cortex and caudate putamen, which was difficult to distinguish in shiverer mice (Fig. 2). The T2 values of the cerebral cortex, white matter, and thalamus of shiverer, heterozygous, and wild-type mice are shown in Table 1. In the white matter, the T2 values of shiverer mice were significantly longer than those of

Table 2
Concentration of metabolites (mean±SD [mM]) in the thalamus and cortex.

		NAA	Cr	Cho	mIns	Gln	Glu
Thalamus	Wt	6.96±0.51	6.95±1.04	2.01±0.09	7.12±0.70	3.50±0.27	8.86±0.41
	Htr	7.17±0.44	7.12±0.39	2.11±0.18 **	7.22±0.46	3.43±0.58	9.08±0.71
	Shi	6.58±0.53	6.97±0.48	1.83±0.07 **	7.17±0.54	3.61±0.41	8.41±0.34
Cortex	Wt	6.80±0.50	6.04±0.65	1.61±0.08	6.05±0.60	3.26±0.32	9.69±0.81
	Htr	6.45±0.48 **	6.04±0.32	1.57±0.09 **	5.91±0.54	3.19±0.42	9.28±1.07 **
	Shi	5.81±0.57 *	6.06±0.36	1.37±0.10 **	6.22±0.36	2.98±0.29	8.02±0.34 **

Mean±SD **,P<0.01 ; *,P<0.05

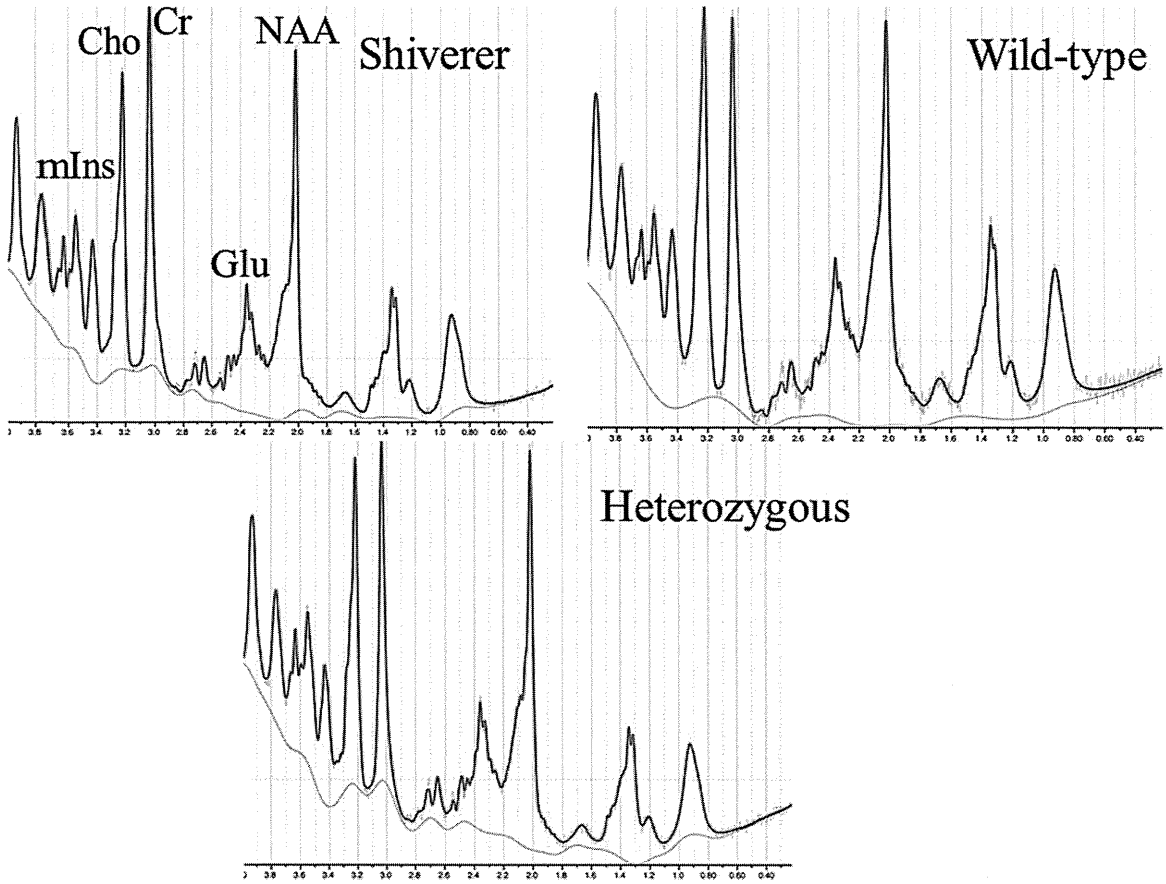

Figure 3. ^{1}H-MRS of the thalamus of shiverer mice shows reduced Cho compared with heterozygous and wild-type mice. [Color figure can be viewed in the online issue, which is available atwileyonlinelibrary.com.]

heterozygous and wild-type mice. In the cortex and thalamus, there were no differences in the T2 values among shiverer, heterozygous, and wild-type mice. Atrophic change, which may affect the concentrations of metabolite measured by water scaling methods, was not observed in either ROI.

Brain Metabolites Measured by ^{1}H-MRS

The concentrations of each metabolite in the thalamus and cortex of shiverer, heterozygous, and wild-type mice are shown in Table 2. The %SD of tNAA, Cr, Cho, mIns, and Glu in all mice were less than 5, and the mean %SD of these metabolites were less than 4 in the three groups. The %SD of Gln was less than 13, and the mean %SD was less than 10 in the three groups.

The two-way ANOVA showed significance in the main effect of the measurement sites and the groups on tNAA and Cho; significance in the main effect of the measurement sites on Cr, mIns, and Gln; and significance in the main effect and the interaction of the groups on Glu. In the thalamus, Cho was decreased in shiverer mice, compared with heterozygous and wild-type mice (Fig. 3). There were no differences in the other metabolites among the three groups. In the cortex, tNAA, Cho, and Glu were decreased in shiverer mice, compared with heterozygous and wild-type mice. There were no differences in these metabolites between heterozygous and wild-type mice; and no differences in Cr, mIns, and Gln between the three groups.

Histological and Immunohistochemical Analyses

The results of histological and immunohistochemical analyses are summarized in Table 3 and Figs. 4 and 5. LFB staining and immunostaining of Mbp, a marker for mature myelin sheaths, in shiverer mice (Fig. 4a,d) revealed sparse and weak staining in the white matter, thalamus, and cortex in comparison with heterozygous (Fig. 4b,e) and wild-type mice (Fig. 4c,f). These findings indicated hypomyelination in the

Table 3
LFB staining and immunohistochemical analyses.

	Shiverer	Heterozygous	Wild-type
LFB	- (GM,WM,Th)	++	++
Mbp	- (GM,WM,Th)	+ (GM,WM,Th)	++
GFAP	+++ (WM)	++	++
Oligo-2	+++ (WM)	++	++
NeuN	+ (GM)	++	++

GM, gray matter; WM, white matter; Th, thalamus; (-), almost no staining; (+), staining less than wild-type mice; (++), staining similar to wild-type mice; (+++), staining stronger than wild-type mice.

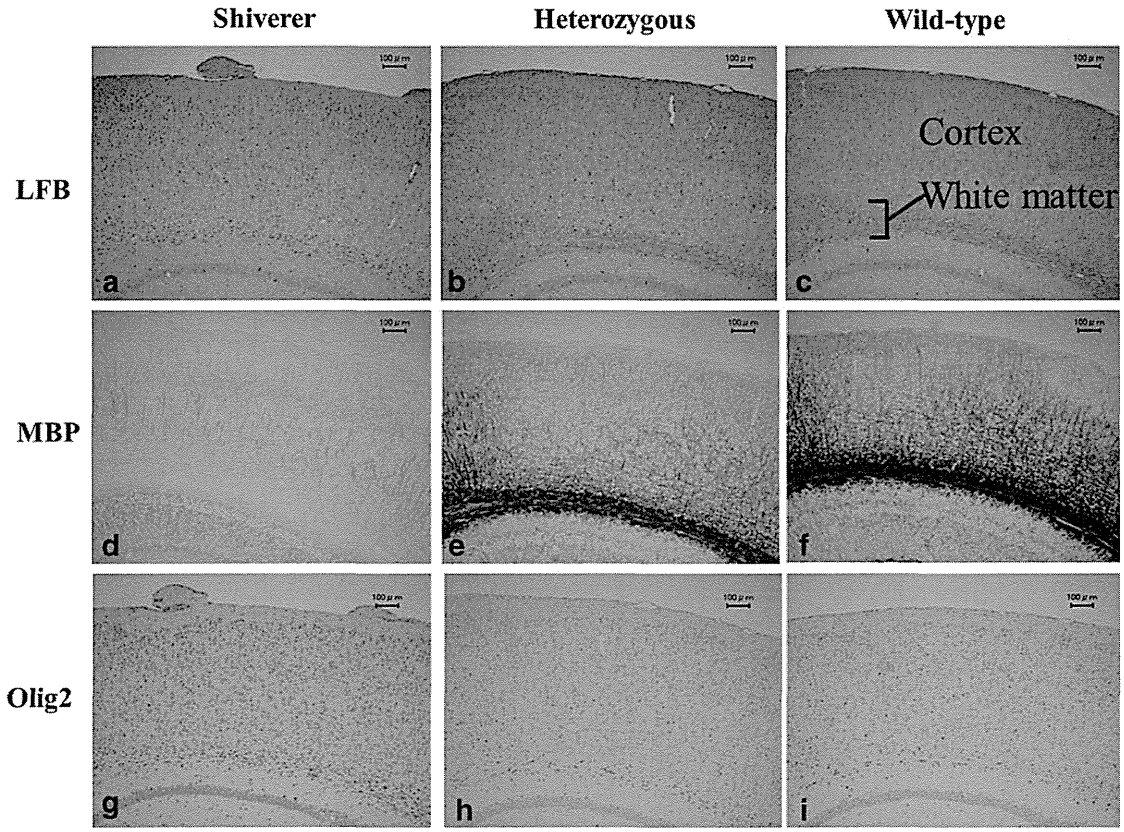

Figure 4. LFB staining and immunostaining of Mbp in shiverer mice (**a,d**) revealed sparse and weak staining in the white matter and cortex in comparison with heterozygous (**b,e**) and wild-type mice (**c,f**), indicating hypomyelination. Immunostaining of Mbp in heterozygous mice (**e**) showed slightly reduced immunoactivity in all regions, compared with wild-type mice (**f**). Olig2 immunostaining of shiverer mice (**g**) revealed increased immunoreactivity in the white matter, compared with heterozygous (**h**) and wild-type mice (**i**), showing an increased number of total oligodendrocytes (OPCs and mature oligodendrocytes). Scale bars = 100 μm.

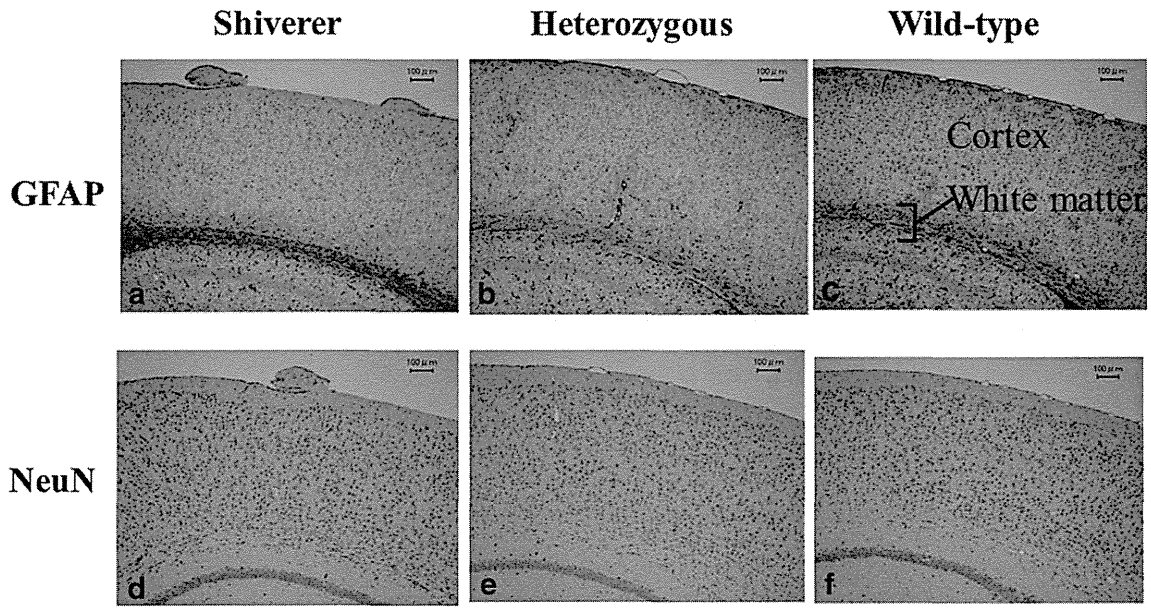

Figure 5. Gfap immunostaining of the shiverer mice (**a**) showed dense and strong staining in the white matter compared with heterozygous and wild-type mice (**b,c**), indicating astrogliosis in the white matter of shiverer mice. NeuN immunostaining of shiverer mice (**d**) revealed decreased immunoreactivity in the cortex (especially on its surface) compared with heterozygous and wild-type mice (**e,f**). Scale bars = 100 μm.

shiverer mice brains at 12W. Immunostaining of Mbp in heterozygous mice (Fig. 4e) showed slightly reduced immunoactivity in all regions, compared with wild-type mice (Fig. 4f). Gfap immunostaining, a marker for astrocytes, of the shiverer mice (Fig. 5a) showed dense and strong staining in the white matter compared with heterozygous and wild-type mice (Fig. 5b,c), indicating astrogliosis in the white matter of shiverer mice. Olig2 immunostaining, a marker for both mature and immature oligodendrocytes of shiverer mice (Fig. 4g), revealed increased immunoreactivity in the white matter, compared with heterozygous and wild-type mice (Fig. 4h,i). The number of the Olig2-positive cells in the white matter was more in shiverer mice (1460, 1220 cells/mm^2) than heterozygous (560, 620 cells/mm^2) and wild-type mice (420, 520 cells/mm^2). This indicated an increased number of total oligodendrocytes (oligodendrocyte progenitor cells [OPCs] and mature oligodendrocytes) in the white matter of shiverer mice. There were no obvious differences in Gfap and Olig2 immunostaining in the thalamus and the cortex between the three groups. NeuN immunostaining, a marker for neuronal cells of shiverer mice (Fig. 5d), revealed decreased immunoreactivity in the cortex (especially on its surface), compared with heterozygous and wild-type mice (Fig. 5e,f), but no obvious difference in the thalamus or white matter.

DISCUSSION

^{1}H-MRS in the thalamus of shiverer mice with the *mbp* mutation revealed a decrease in Cho with normal tNAA, which is distinct from in *msd* mice with the *plp1* mutation that show a decrease in Cho with an increase in tNAA (6). These findings suggest that increased tNAA is not directly related to hypomyelination. NeuN immunostaining (a marker for neuronal cells) of the thalamus in both shiverer and *msd* mice revealed no difference compared with wild-type mice; therefore, the number of neuronal cells in the thalamus seems unlikely to explain the difference in tNAA.

What is the cause of the difference in tNAA observed on ^{1}H-MRS between the two hypomyelinating strains? Mbp immunostaining indicated hypomyelination in the shiverer mice brain, as observed in the *msd* mice brain (6). Reflecting the pathology, shiverer mice exhibited longer T2 values than heterozygous and wild-type mice in the white matter, as also observed in *msd* mice brain (6). Mutant plp1 proteins in *msd* mice are abnormally folded and accumulated in the endoplasmic reticulum, resulting in the activation of an unfolded protein response that finally leads to oligodendrocyte apoptotic death before normal myelination occurs (13). In *msd* and also in another PMD mouse model, *jimpy*, massive apoptosis of oligodendrocytes appears to induce proliferation of OPCs in the white matter (14,15), leading to an increase of OPCs and the absence of mature oligodendrocytes. On the other hand, the absence of mbp protein in shiverer mice results in the failure of oligodendrocytes to form a compact myelin sheath. Unlike in *msd* and *jumpy* mice, OPCs in shiverer mice can differentiate into oligodendrocytes, and both OPCs and mature oligodendrocytes are increased in number by as much as two times (16), as shown on Olig2 immunostaining (Fig. 4g). One possible explanation for the difference in tNAA is the different patterns of oligodendrocytes in shiverer and *msd* mice.

NAA is one of the most highly abundant free amino acids in the CNS (around 10 mM in man), and it is generally considered to be an important marker of neurons and axons (8,9). NAA is either released from neurons or transported to oligodendrocytes, where it is catabolized by aspartoacylase into acetate and aspartate (17), which are used for fatty acid and steroid synthesis, and energy production, respectively. In *msd* mice, the absence or dysfunction of mature oligodendrocytes may either disable neuron-to-oligodendrocyte NAA transport or affect NAA catabolism in oligodendrocytes, leading to NAA accumulation in neurons. An elevated NAA concentration also increases NAAG biosynthesis (9), which probably results in increased tNAA on ^{1}H-MRS. On the other hand, NAA in shiverer mice may be normally transported from neurons to oligodendrocytes, and then catabolized into acetate and aspartate, leading to normal tNAA on ^{1}H-MRS. In the cortex of shiverer mice, tNAA is decreased compared with wild-type and heterozygous mice, probably reflecting the decreased number of neuronal cells in shiverer mice, as shown on NeuN immunostaining. The majority of excitatory neurons in the cerebral cortex release Glu, which is taken up from the synaptic cleft by surrounding astrocytes and metabolized into a relatively harmless compound, Gln. Therefore, Glu and Gln are considered to be markers of neurons and astrocytes, respectively. The decrease of Glu in the cortex of shiverer mice supports the theory that a decrease in tNAA reflects a decreased number of neuronal cells.

Another detectable metabolic change in shiverer mice is a reduction of Cho, which is also observed in *msd* mice (6) and patients with PMD (7). However, the degree of Cho reduction in the thalamus of shiverer mice compared with that in wild-type mice (−6.6%) is much less than that in *msd* mice (−21.8%). The Cho peak likely contains various cell membrane precursors or breakdown products such as phosphocholine, glycerophosphocholine, and phosphatidylcholine. Thus, Cho increases in association with accelerated myelination in infantile brains (18), and probably decreases in association with the severe retardation of myelination. ^{1}H-MRS in vitro demonstrated that cultured oligodendrocytes per se had a higher concentration of Cho than neurons, astrocytes, and OPCs (19,20). The different degrees of Cho reduction in the two hypomyelination strains may be explained by the pathological difference of oligodendrocytes, that is, severe hypomyelination with an increased number of oligodendrocytes in shiverer mice (16), leading to a mild reduction of Cho, and the severe hypomyelination with the absence of oligodendrocytes in *msd* mice (14), resulting in a severer reduction of Cho. Whatever the cause, the reduction of

Cho might be a marker for hypomyelinating disorders on ^{1}H-MRS.

Heterozygous mice (*shi/+*) have been reported to be clinically asymptomatic, and to exhibit normal brain MRI (21,22). They also have been shown to have normal myelin sheaths by electron microscopic studies of optic nerves, although the Mbp gene expression level is 50% of normal (21), which reasonably leads to slightly reduced immunoactivity of Mbp (Fig. 4e) compared with wild-type mice. Heterozygous mice, however, exhibit a 7% increase in visually evoked potential latency, suggesting mild optic nerve dysfunction compared with wild-type mice (23). Mildly increased Cho in thalami of heterozygous mice (+5.1%), compared with wild-type mice, might also reflect a subtle myelin dysfunction, most probably increased turnover of oligodendrocytes or myelination itself.

^{1}H-MRS showed no difference in Cr among the three groups, although increased Cr has been reported in *msd* mice (6) and patients with PMD (7). The Cr peak is composed of proton resonances from both phosphocreatine and free Cr, which are involved in energy metabolism, and are present in both neuronal and glial cells. In rats, astrocytes have Cr concentrations twice as high as those observed in neurons (19). As reactive astrogliosis is observed in the *msd* mouse brain (6), the elevated Cr was considered to result from the increased number of astrocytes. Absence of any obvious difference in Gfap immunostaining (a marker for astrocytes) in the thalamus and cortex among shiverer, heterozygous, and wild-type mice is, therefore, the likely reason for the absence of difference in Cr concentration.

Some aspects of the ^{1}H-MRS in this study require discussion. Because the white matter of mice is very thin, attempts to place the ROI in the white matter result in both inadequate signal-to-noise and contamination from the adjacent cortex and deep gray nuclei. The normal thalamus is composed of a mixture of myelinated axons and neurons; therefore, ^{1}H-MRS in shiverer mice may reflect metabolic derangements of both components. Mbp immunostaining indicated hypomyelination in both the white matter and thalamus of the shiverer brain. In addition, the number of neurons in the thalamus was almost the same in shiverer, heterozygous, and wild-type mice. These suggest that ^{1}H-MRS in the thalamus reasonably reflects the metabolic derangements associated with hypomyelination. A limitation should also be mentioned regarding the pathologic examinations in this study. Only two mice of each group were pathologically examined with qualitative evaluation. The G-ratio, the ratio between axon diameter and fiber diameter (axon diameter + myelin sheath thickness) (24), sometimes used for the detailed analysis of myelination, was not evaluated in this study.

In conclusion, this study revealed a reduction of Cho with normal tNAA level in the thalamus of the shiverer mouse (a hypomyelination mutant with the absence of *mbp*). The presence of mature oligodendrocytes in shiverer mice, which enable neuron-to-oligodendrocyte NAA transport or NAA catabolism, may result in a normal tNAA level in contradistinction to the *msd* mouse (a hypomyelination mutant with absence of *plp1*). Although tNAA seems to vary depending on the underlying pathology, reduction of Cho observed on ^{1}H-MRS might be a common marker for hypomyelinating disorders.

ACKNOWLEDGMENTS

We thank Ms. Sayaka Shibata (Molecular Imaging Center, National Institute of Radiological Sciences, Chiba, Japan) for technical support; and Dr. Masaharu Hayashi (Department of Brain Development and Neural Regeneration, Tokyo Metropolitan Institute of Medical Science, Tokyo, Japan) and Dr. Kazuhiko Sawada (Faculty of Medical and Health Sciences, Tsukuba International University, Tsuchiura, Japan) for comments on pathology.

REFERENCES

1. Nave KA. Neurological mouse mutants and the genes of myelin. J Neurosci Res 1994;38:607–612.
2. Readhead C, Hood L. The dysmyelinating mouse mutants shiverer (shi) and myelin deficient (shi^{mld}). Behav Genet 1990;20: 213–234.
3. Campagnoni AT. Molecular biology of myelin proteins from the central nervous system. J Neurochem 1988;51:1–14.
4. Takanashi J, Sugita K, Tanabe Y, et al. MR-revealed myelination in the cerebral corticospinal tract as a marker for Pelizaeus-Merzbacher disease with proteolipid protein gene duplication. AJNR Am J Neuroradiol 1999;20:1822–1828.
5. Inoue K. PLP1-related inherited dysmyelinating disorders: Pelizaeus-Merzbacher disease and spastic paraplegia type 2. Neurogenetics 2005;6:1–16.
6. Takanashi J, Saito S, Aoki I, Barkovich AJ, Ito Y, Inoue K. Increased N-acetylaspartate in model mouse of Pelizaeus-Merzbacher disease. J Magn Reson Imaging 2012;35:418–425.
7. Takanashi J, Inoue K, Tomita M, et al. Brain N-acetylaspartate is elevated in Pelizaeus-Merzbacher disease with PLP1 duplication. Neurology 2002;58:237–241.
8. Moffett JR, Namboodiri MAA. Expression of N-acetylaspartate and N-acetylaspartylglutamate in nervous system. Adv Exp Med Biol 2006;576:7–26.
9. Moffett JR, Ross B, Arun P, Madhavarao CN, Namboodiri AM. N-acetylaspartate in the CNS: from neurodiagnostics to neurobiology. Prog Neurobiol 2007;81:89–131.
10. Takanashi J, Somazawa F, Maruyama K,Terada H, Xu D, Barkovich AJ. Metabolic changes in early childhood using LCModel with corrected water scaling method. J Magn Reson Imaging 2012;35:174–180.
11. Atwood T, Robbins ME, Zhu J-M. Quantitative in vivo proton MR spectroscopic evaluation of the irradiated rat brain. J Magn Reson Imaging 2007;26:1590–1595.
12. Provencher SW. LCModel & LCMgui user's manual. http://s-provencher.com/pub/LCModel/manual/manual.pdf 2013.
13. Gow A, Southwood CM, Lazzarini RA. Disrupted proteolipid protein trafficking results in oligodendrocyte apoptosis in an animal model of Pelizaeus-Merzbacher disease. J Cell Biol 1998;140: 925–934.
14. Skoff RP. Increased proliferation of oligodendrocytes in the hypomyelinating mouse mutant-jimpy. Brain Res 1982;248:19–31.
15. Nishiyama A. Glial progenitor cells in normal and pathological states. Keio J Med 1998;47:205–208.
16. Bu J, Banki A, Wu Q, Nishiyama A. Increased NG2$^+$ glial cell proliferation and oligodendrocyte generation in the hypomyelinating mutant shiverer. Glia 2004;48:51–63.
17. Bhakoo KK, Craig TJ, Styles P. Developmental and regional distribution of aspartoacylase in rat brain tissue. J Neurochem 2001; 79:211–220.
18. Grodd W, Krageloh-Mann I, Klose U, Sauter R. Metabolic and destructive brain disorders in children: findings with localized proton MR spectroscopy. Radiology 1991;181:173–181.

19. Urenjak J, Williams SR, Gadian DG, Noble M. Proton nuclear magnetic resonance spectroscopy unambiguously identifies different neural cell types. J Neurosci 1993;13:981–989.
20. Jansen JFA, Shamblott MJ, van Zijl PCM, et al. Stem cell profiling by nuclear magnetic resonance spectroscopy. Magn Reson Med 2006;56:666–670.
21. Shine HD, Readhead C, Popko B, Hood L, Sidman RL. Morphometric analysis of normal, mutant, and transgenic CNS: correlation of myelin basic protein expression to myelinogenesis. J Neurochem 1992;58:342–349.
22. Tanaka R, Iwasaki N, Hayashi M, et al. Abnormal brain MRI signal in 18q- syndrome not due to dysmyelination. Brain Dev 2012;34:234–237.
23. Martin M, Hiltner TD, Wood JC, Fraser SE, Jacobs RE, Readhead C. Myelin deficiencies visualized in vivo: visually evoked potentials and T2-weighted magnetic resonance images of shiverer mutant and wild-type mice. J Neurosci Res 2006;84:1716–1726.
24. Chomiak T, Hu B. What is the optimal value of the g-ratio for myelinated fibers in the rat CNS? A theoretical approach. PLoS One 2009;4:e7754.

Journal of Controlled Release 174 (2014) 63–71

Contents lists available at ScienceDirect

Journal of Controlled Release

journal homepage: www.elsevier.com/locate/jconrel

Hydrothermally synthesized PEGylated calcium phosphate nanoparticles incorporating Gd-DTPA for contrast enhanced MRI diagnosis of solid tumors

Peng Mi [a,b], Daisuke Kokuryo [c], Horacio Cabral [a], Michiaki Kumagai [d], Takahiro Nomoto [a], Ichio Aoki [c], Yasuko Terada [e], Akihiro Kishimura [f], Nobuhiro Nishiyama [b,*], Kazunori Kataoka [a,d,f,**]

[a] Department of Bioengineering, Graduate School of Engineering, The University of Tokyo, 7-3-1 Hongo, Bunkyo-ku, Tokyo 113–8656, Japan
[b] Polymer Chemistry Division, Chemical Resources Laboratory, Tokyo Institute of Technology, R1-11, 4259 Nagatsuta, Midori-ku, Yokohama 226–8503, Japan
[c] Molecular Imaging Center, National Institute of Radiological Sciences, Anagawa 4-9-1, Inage, Chiba, 263–8555, Japan
[d] Center for Disease Biology and Integrative Medicine, Graduate School of Medicine, The University of Tokyo, 7-3-1 Hongo, Bunkyo-ku, Tokyo 113–0033, Japan
[e] SPring 8, JASRI, 1-1-1 Kouto, Sayo-cho, Sayo-gun, Hyogo 679–5198, Japan
[f] Department of Materials Engineering, Graduate School of Engineering, The University of Tokyo, 7-3-1 Hongo, Bunkyo-ku, Tokyo 113–8656, Japan

ARTICLE INFO

Article history:
Received 18 July 2013
Accepted 28 October 2013
Available online 6 November 2013

Keywords:
Calcium phosphate nanoparticles
Block copolymer
Hydrothermal synthesis
MRI
Gd-DTPA
Cancer diagnosis

ABSTRACT

Organic–inorganic hybrid nanoparticles with calcium phosphate (CaP) core and PEGylated shell were developed to incorporate magnetic resonance imaging (MRI) contrast agent diethylenetriaminepentaacetic acid gadolinium (III) (Gd-DTPA) for noninvasive diagnosis of solid tumors. A two-step preparation method was applied to elaborate hybrid nanoparticles with a z-average hydrodynamic diameter about 80 nm, neutral surface ξ-potential and high colloidal stability in physiological environments by self-assembly of poly(ethylene glycol)-*b*-poly(aspartic acid) block copolymer, Gd-DTPA, and CaP in aqueous solution, followed with hydrothermal treatment. Incorporation into the hybrid nanoparticles allowed Gd-DTPA to show significant enhanced retention ratio in blood circulation, leading to high accumulation in tumor positions due to enhanced permeability and retention (EPR) effect. Moreover, Gd-DTPA revealed above 6 times increase of relaxivity in the nanoparticle system compared to free form, and eventually, selective and elevated contrast enhancements in the tumor positions were observed. These results indicate the high potential of Gd-DTPA-loaded PEGylated CaP nanoparticles as a novel contrast agent for noninvasive cancer diagnosis.

1. Introduction

Precise diagnosis of malignant tumors is essential for proper clinical treatments, and several diagnostic imaging methods have been applied. Among these, MRI can noninvasively provide highly quantitative and qualitative anatomical details of soft tissues [1]. In clinical, small paramagnetic molecules, especially Gd (III) based T_1 contrast agents are usually used for MRI measurements to improve the contrast of tissues, as the gadolinium complexes are stable and maintain strongly paramagnetic properties [2,3]. Nevertheless, tumor imaging using current clinically used contrast agents is often limited, because of their fast clearance from blood stream and low-tissue specificity, leading to inadequate sensitivity, specificity and spatial resolution [4]. Therefore, development of highly sensitive and tumor specific MRI probes has advocated much interest for cancer diagnosis. Accordingly, a myriad of nanoparticles have been considered as delivery carriers of contrast agents to optimize their pharmacokinetic properties for experimental or preclinical detection of solid tumors, such as polymeric micelles [5–10], liposomes [11,12], polymersomes [13,14], iron oxide nanoparticles [1,15,16], lipid nanoparticles [17–19] and other nanoscaffolds [20–23]. These nanoscale MRI probes have shown greater tumor selectivity than low molecular weight contrast compounds, owing to their ability to leak from the hyperpermeable vasculature of tumors and be retained in tumor tissues due to ineffective lymphatic drainage, which is known as the EPR effect [24]. Moreover, nanoscale MRI probes can provide higher sensitivity by increasing the relaxivity of the incorporated contrast agents due to decreased molecular tumbling rates [21,25,26]. In addition, they can combine their tumor imaging capability with cellular targeting and therapeutic activity by decorating the surface with ligands and incorporating bioactive molecules, respectively [27,28]. Development of efficient and safe nanocarriers for *in vivo* MR cancer detection could have a significant impact on human health care, owing to the widely clinical setting of MRI as well as the progressive increasing of cancer incidences all over the world [29].

* Correspondence to: N. Nishiyama, Polymer Chemistry Division, Chemical Resources Laboratory, Tokyo Institute of Technology, R1-11, 4259 Nagatsuta, Midori-ku, Yokohama 226–8503, Japan. Tel.: +81 45 924 5240; fax: +81 45 924 5275.
** Correspondence to: K. Kataoka, Department of Materials Engineering, Graduate School of Engineering, The University of Tokyo, 7-3-1 Hongo, Bunkyo-ku, Tokyo 113–8656, Japan. Tel.: +81 3 5841 7138; fax: +81 3 5841 7139.
E-mail addresses: nishiyama@res.titech.ac.jp (N. Nishiyama), kataoka@bmw.t.u-tokyo.ac.jp (K. Kataoka).

0168-3659/$ – see front matter © 2013 Elsevier B.V. All rights reserved.
http://dx.doi.org/10.1016/j.jconrel.2013.10.038

CaP-based drug delivery systems, firstly reported as carriers to enhance DNA transfection into mammalian cells before [30], attracted increasing interests in recent years because of its adequate biodegradation and excellent biocompatibility [31–34]. Many biochemical compounds can be incorporated in the solid framework of CaP nanoparticles to obtain improved functions. CaP nanoparticles can be prepared by various synthetic methods, including microemulsion [35,36], layer-by-layer [37,38] and wet chemical routes [39,40]. For some preparation procedures, it is usually difficult to control the crystal growth and the size of nanoparticles as well as prevent agglomeration. Moreover, for microemulsion synthetic route, which can achieve size control and colloidal stability, it is difficult to completely remove the synthetic precursors, especially some toxic agents like cyclohexane, and demulsification of nanoparticles may occur during purification [32].

We have pioneered the procedure to form PEGylated CaP nanoparticles with controlled size and appreciable colloidal stability by self-assembly in aqueous phase of CaP with PEG-polyanion block copolymers, such as poly(ethylene glycol)-*b*-poly(aspartic acid) (PEG-*b*-PAsp) [41]. In this way, organic–inorganic hybrid nanoparticles were formed with precise control of the growth of CaP crystal, as the anionic blocks of the copolymers interact with CaP inhibiting further growth of crystal, while PEG units decorate the surface of nanoparticles avoiding aggregation between CaP particles [42–44]. This PEG shield also protects the drug-loaded core during transportation in biological environments. By this method, we have successfully incorporated small interfering RNA (siRNA) or DNA inside CaP hybrid nanoparticles as non-viral gene carriers and achieved efficient transfection efficiency, demonstrating promising application for gene therapy [45–47]. Nevertheless, it is a challenge to load some functional molecules, such as Gd-DTPA, without phosphate groups like siRNA and DNA, to interact with CaP matrix. Besides, high colloidal stability of nanoscale probes for MRI is preferred, as leaking of contrast agents during transportation may lose contrast specificity, and Gd-DTPA has a blood half-time less than 5 min which is insufficient to enhance the contrast of tumor tissues [48]. Thus, developing stable CaP nanoparticles incorporating Gd-DTPA for cancer diagnosis is quite challenging and significant, as CaP based nanocarriers for *in vivo* MRI diagnosis of solid tumors have not been reported yet.

Herein, we designed a facile two-step method to prepare organic–inorganic hybrid CaP nanoparticles stably incorporating Gd-DTPA (Gd-DTPA/CaP) with enhanced relaxivity and physiological stability for noninvasive *in vivo* cancer diagnosis (Fig. 1). Accordingly, spherical and monodispersed Gd-DTPA/CaP were firstly synthesized by a fast homogenous procedure using PEG-*b*-PAsp to prevent the overgrowth of CaP precipitates. Then, Gd-DTPA/CaP was subjected to hydrothermal synthetic process at relatively low temperature of 120 °C to increase the colloidal stability, as hydrothermal treatment is usually used to treat hydroxyapatite materials for orthopedics applications to enhance its mechanical reliability (stability) in wet environments [49]. Prepared Gd-DTPA/CaP was characterized by a series of *in vitro* and *in vivo* experiments, and further used for *in vivo* MRI contrast enhancement of solid tumors.

2. Materials and methods

2.1. Materials, cell line and animals

β-Benzyl-L-aspartate *N*-carboxy-anhydride (BLA-NCA) was obtained from Chuo Kaseihin Co., Inc. (Tokyo, Japan). Dulbecco's Modified Eagle Medium (DMEM), fetal bovine serum (FBS) and Gd-DTPA were purchased from Sigma–Aldrich (St. Louis, Missouri). Gd-DTPA was converted to sodium salt by adjusting the pH to 7 with NaOH and lyophilizing before use. MeO-PEG-NH_2 (Mw = 12,000, Mw/Mn = 1.03) was purchased from Nippon Oil and Fats Co., Ltd. (Tokyo, Japan).

Murine colon adenocarcinoma 26 (C-26) cells were kindly supplied by the National Cancer Center (Tokyo, Japan), and maintained with DMEM supplemented with 10% FBS. Human umbilical vein endothelial cells (HUVEC) and the endothelial cell growth medium-2 (EGM-2) bullet kit were obtained from Lonza Ltd. (Basel, Switzerland). The HUVEC were used for experiments after 10 times passage. All the cells were maintained in the medium and incubated in humidified atmosphere containing 5% CO_2 at 37 °C. Female BALB/c nude mice (6 weeks, 18–20 g) were purchased from Charles River Laboratories, Inc. (Tokyo, Japan), and all the animal experiments were carried out following the policies of the Animal Ethics Committee of the University of Tokyo.

2.2. Synthesis of PEG-b-PAsp

PEG-*b*-PAsp block copolymer with 40 degree of polymerization (DP) for PAsp was synthesized according to the previously described synthetic methods [50]. Briefly, BLA-NCA was polymerized by ring-opening procedures in mixed solvent of DMF and CH_2Cl_2, initiated by the primary amino group of MeO-PEG-NH_2 (M_w = 12,000) to obtain PEG-*b*-poly(β-benzyl-L-aspartate) (PEG-*b*-PBLA) block copolymer. The molecular weight distribution of PEG-*b*-PBLA was M_w/M_n = 1.05, which was determined by gel permeation chromatography (GPC) system (HLC-8220, Tosoh, Japan) equipped with TSK-gel columns (SuperAW3000 and SuperAW4000, Tosoh Bioscience LLC, Tokyo, Japan) and an internal refractive index (RI) detector at 40 °C. *N*-methyl-2-pyrrolidone (NMP) containing LiBr (50 mM) was used as mobile phase and linear PEG standards were used for calibration. The DP was determined to be 40 by

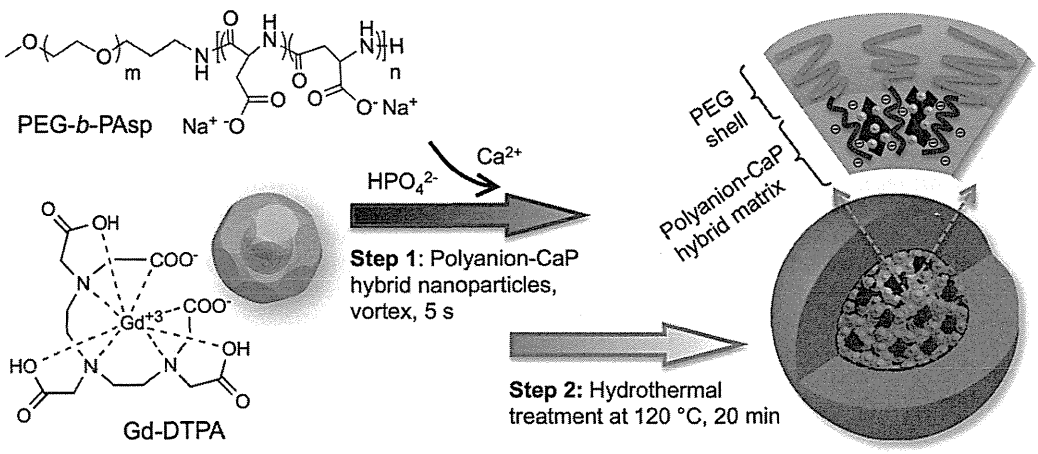

Fig. 1. Scheme showing the design and synthetic procedures of developing Gd-DTPA doped, PEG-*b*-PAsp hybrid calcium phosphate nanoparticles (Gd-DTPA/CaP) following a two-step method of PEG-polyanion controlled preparation in 5 s and hydrothermal treatment at 120 °C for 20 min to enhance the colloidal stability of nanoparticles.

comparing the proton ratios of methylene units in PEG (–OCH_2CH_2–: $\delta = 3.7$ ppm) and phenyl groups of PBLA (–C_6H_5: $\delta = 7.3$ ppm) in ^{1}H-NMR measurement (solvent: DMSO-d_6, temperature: 80 °C). PEG-*b*-PAsp (12 k-40DP) was obtained via removing benzyl groups of PEG-*b*-PBLA, which was carried out by mixing with 0.5 N NaOH (5 eq.) at room temperature and reacted for 1 h, then the block copolymer was dialyzed against Mili-Q water, and finally collected by lyophilization. The deprotection was confirmed by ^{1}H-NMR measurement (solvent: D_2O, temperature: 25 °C).

2.3. Fabrication of Gd-DTPA/CaP

Firstly, 0.1 ml of 2.5 M $CaCl_2$ was diluted in 1 ml Tris–HCl buffer (pH 7.6) (solution A). PEG-*b*-PAsp at the concentration of carboxylic acid groups of PAsp from 3 mM to 6 mM respectively, and Gd-DTPA at a concentration of 2 mM were dispersed in 50 mM HEPES saline buffer (pH 7.1, NaCl 140 mM) containing 6 mM Na_2HPO_4 (solution B). Equal volume of solution B was quickly added to solution A with vigorous stirring by a vortex mixer for 5 s. Then, Gd-DTPA/CaP nanoparticles were treated by hydrothermal synthesis for 20 min at 120 °C using an autoclave machine under the pressure of 100 kPa. The hydrothermal treated Gd-DTPA/CaP nanoparticles were purified by dialysis and ultrafiltration (MWCO: 100,000) using 25 mM HEPES saline buffer (pH 7.4, NaCl 140 mM and 2 mM $CaCl_2$). Gd-DTPA/CaP nanoparticles without hydrothermal treatment were also purified as above described as control.

2.4. Characterization of Gd-DTPA/CaP

Size distribution of obtained Gd-DTPA/CaP nanoparticles was evaluated by dynamic light scattering (DLS) measurement using a Zetasizer Nano ZS90 (Malvern Instruments, UK). The amount of Gd-DTPA incorporated in CaP nanoparticles was determined by ICP-MS (4500 ICP-MS, Hewlett Packard, Delaware, USA). Then, 1 ml of Gd-DTPA/CaP nanoparticles was lyophilized and the weight was measured to calculate the loading efficacy. Meanwhile, 1 ml of Gd-DTPA/CaP nanoparticles was dialyzed (MWCO: 6000–8000) in 5 L of Mili-Q water and the water was changed for several times. The existence of nanoparticles was checked by DLS and, 72 h later, the inner solution of dialysis bag was lyophilized and the weight was measured to calculate the composition of block copolymer. The morphology of Gd-DTPA/CaP nanoparticles was investigated using TEM (JEM-1400, JEOL, Tokyo, Japan). The hydroxyapatite crystal line of the obtained product was characterized by X-ray diffraction (XRD) (PW18v5/20, Philips, Amsterdam, Netherlands) with Cu-Kα incident radiation. The proton longitudinal relaxation rate r_1 of Gd-DTPA/CaP and Gd-DTPA was measured in 10 mM PBS buffer (pH 7.4, NaCl 140 mM) at 37 °C by utilizing ^{1}H-NMR analyzer (JNM-MU25A, JEOL, Tokyo, Japan) at 0.59 T. The longitudinal relaxation time T_1 (s) was measured by inversion-recovery pulse sequence method. The T_1 (s) values of 0.2, 0.4, 0.6, 0.8 and 1.0 mM Gd-DTPA and Gd-DTPA/CaP were measured and the r_1 relaxivity was calculated from the equation of $r_1 = (1/T_1 - 1/T_{1(0)})/[\mathrm{Gd}]$, where [Gd] is the concentration of paramagnetic CAs (mM), $1/T_{1(0)}$ (s^{-1}) is the longitudinal relaxation rate contrast in the absence of a paramagnetic species, and $1/T_1$ (s^{-1}) is the longitudinal relaxation rate contrast in the presence of a paramagnetic species. Moreover, equal volume of solutions containing 0.1, 0.2, 0.3 and 0.4 mM Gd-DTPA or Gd-DTPA/CaP in saline buffer were placed in thin-wall PCR tubes, respectively, and then closed with flat caps for MR imaging at 1 T (Aspect, Aspect Imaging).

2.5. Physicochemical characterization

Gd-DTPA released from Gd-DTPA/CaP was measured by dialysis of Gd-DTPA/CaP in 10 mM PBS buffer (pH 7.4, NaCl 140 mM) incubated at 37 °C with shaking. One-tenth milliliter of outer solution was sampled at defined time, and the concentration of Gd-DTPA was measured by ICP-MS. To study the stability of Gd-DTPA/CaP, the samples were washed with methanol to remove free Ca^{2+} ions in the buffer by ultrafiltration, and finally washed with 10 mM PBS buffer (pH 7.4, NaCl 140 mM). Then, samples were incubated in physiological environments (10 mM PBS buffer containing 140 mM NaCl, pH 7.4 and 37 °C) and characterized by DLS and static light scattering (SLS) using a Photal dynamic laser light scattering spectrophotometer (Photal DLS-7000, Otsuka Electronics). The ξ-potential of Gd-DTPA/CaP nanoparticles was measured in 10 mM phosphate buffer (pH 7.4) using Zetasizer Nano ZS90.

2.6. Cytotoxicity study

To determine the cytotoxicity of Gd-DTPA/CaP and Gd-DTPA, HUVEC and C-26 cells were seeded in 96 well plates and incubated respectively. Twenty-four hours later, the cells were exposed to free Gd-DTPA or Gd-DTPA/CaP for 72 h, followed by adding Cell Counting Kit-8 solution (Dojindo Molecular Technologies, Inc., Japan). The cell viability in each plate was measured using a micro-plate reader (Model 680, Bio-Rad Laboratories, Inc., Hercules, US) at 450 nm.

2.7. In vivo biodistribution assay

Female BALB/c nude mice were inoculated subcutaneously with 100 μl of C-26 tumor cells at a concentration of 1×10^6 cell/ml to prepare subcutaneous tumor models. When the subcutaneous tumor volume reached 100 mm^3, Gd-DTPA/CaP and free Gd-DTPA were intravenously injected to C-26 tumor-bearing mice at a dose of 0.02 mmol/kg based on Gd-DTPA. Then, tumor and major organs were harvested at 1, 4, 8 and 24 h. Meanwhile, blood was collected from the inferior vena cava, heparinized and centrifuged to obtain the plasma. The plasma and all organs were dissolved in 90% HNO_3, evaporated and re-dissolved in 1% HNO_3 solution to prepare samples for ICP-MS measurement. Moreover, equal dose of Gd-DTPA and Gd-DTPA/CaP was intravenously injected to C-26 subcutaneous tumor-bearing mice. The tumor tissues were harvested, immediately put into OCT compound, and then frozen in acetone/dry ice mixture. The frozen samples were further cut to 16-μm thickness in a cryostat (CM1950, Leica, Germany). Next, some sections were fixed and stained with hematoxylin and eosin (H&E) and then samples were observed by using an AX80 microscope (Olympus, Japan). Other tumor tissue sections were scanned by micro-synchrotron radiation-induced X-ray fluorescence spectrometry (μ-SR-XRF) using beamline 37XU in SPring-8 (Hyogo, Japan) with 14 keV of energy and an intensity of 1×10^{12} photons per second to determine distributions of Gd, Ca and Fe elements in tumor sections [51].

2.8. MRI measurements

BALB/c nude mice (female, 6 weeks) were inoculated subcutaneously with C-26 cells to prepare tumor models for MRI measurements. *In vivo* MR imaging of the tumors was conducted with a 1 T imaging spectrometer (Aspect, Aspect Imaging) until the mean tumor volume reached 100 mm^3. Gd-DTPA/CaP was intravenously injected to C-26 subcutaneous tumor bearing mice at a dose of 0.05 mmol/kg based on Gd-DTPA for MRI imaging with anesthesia, while *in vivo* MRI administrated with Gd-DTPA at a dose of 0.22 mmol/kg was measured as control. For the T_1-weighted MR imaging of live mice, the following parameters were adopted: spin-echo method, repetition time (TR) = 400 ms, echo time (TE) = 11 ms, field of view (FOV) = 48 × 48 mm, matrix size = 256 × 256, and slice thickness = 2 mm.

Table 1
Size and distribution of Gd-DTPA/CaP nanoparticles measured by DLS.

Concentration of COO^- from PEG-*b*-PAsp (mM)[a]	Z-average diameter (nm)	Polydispersity index (PDI)
3	565 ± 19	0.59 ± 0.04
4	190 ± 16	0.26 ± 0.03
5	76 ± 10	0.14 ± 0.02
6	78 ± 6	0.17 ± 0.02

[a] The concentration of Gd-DTPA was fixed at 2 mM.

3. Results and discussion

3.1. Fabrication and characterization of Gd-DTPA/CaP nanoparticles

For *in vivo* applications, homogeneous and small sizes of CaP nanoparticles are preferred, while a PEGylated surface increases the biocompatibility of nanoparticles. To achieve this, a simple two-step method was adopted for preparing Gd-DTPA/CaP nanoparticles. In the first homogenous preparation step, Gd-DTPA/CaP nanoparticles were prepared by mixing Tris–HCl solution containing 250 mM Ca^{2+} and HEPES solution containing 6 mM HPO_4^{2+}, 2 mM Gd-DTPA and varying concentration of PEG-*b*-PAsp block copolymer with vigorous shaking using vortex mixer. Considering stability of CaP prepared at room temperature was not high [52], we treated the solution of Gd-DTPA/CaP nanoparticles at 120 °C for 20 min under a pressure of 100 kPa for hydrothermal treatment to increase their colloidal stability. Hydrothermal treatment at elevated temperature and pressure is often used to modulate the properties of inorganic materials, for instance, to treat hydroxyapatite based biomaterials for orthopedic applications to increase the crystallinity, thereby improving the mechanical reliability in wet environments [49,52,53].

As shown in Table 1, increase in the concentration of carboxylic acid groups of PEG-*b*-PAsp from 3 mM to 6 mM caused dramatic decrease in the hydrodynamic diameter of Gd-DTPA/CaP from over 565 nm to sub-100 nm while reducing polydispersity index (PDI). This trend was maintained until the nanoparticles reached approximately 76 nm using 5 mM carboxylate solution of PEG-*b*-PAsp (Fig. 2A). Hydrothermal treatment induces no significant change in the size and PDI of Gd-DTPA/CaP samples, and there was only a very slight increase in the average size to 80 nm after purification. Then, freeze-dried sample of Gd-DTPA/CaP nanoparticles with hydrothermal treatment was analyzed by X-ray diffraction pattern (XRD) measurement, and typical peaks of hydroxylapatite crystal were found (Fig. 2B), demonstrating the existence of $Ca_{10}(PO_4)_6(OH)_2$ [49,52]. Inside Gd-DTPA/CaP nanoparticles, the organic parts (block copolymer and Gd-DTPA) composed up to near 30% (weight/weight) and the content of Gd-DTPA was approximately 2.5% of the whole weight.

The Gd-DTPA/CaP samples obtained without hydrothermal treatment were not stable even during purification procedures (dialysis and ultrafiltration). Size evaluation by DLS gave a broad size distribution and some of those nanoparticles were broken according to TEM image shown in Fig. 2C. The morphology of Gd-DTPA/CaP nanoparticles with hydrothermal treatment was also studied by transmission electron microscopy (TEM), as shown in Fig. 2D. The spherical morphology and monodispersity of Gd-DTPA/CaP were confirmed from TEM images (Fig. 2D), and the size was calculated to be nearly 55 nm (Fig. 2E), which might correspond to the core size of Gd-DTPA/CaP as it is difficult to stain and detect their PEG layer by TEM. Moreover, no agglomeration of nanoparticles was observed from all of the TEM images, which may result from the efficient PEG surface decoration of the organic–inorganic hybrid structure prohibiting Gd-DTPA/CaP nanoparticles interact with each other, as we also confirmed that surface ξ-potential of Gd-DTPA/CaP was almost neutral (−0.5 mV). Therefore, hydrothermal treatment

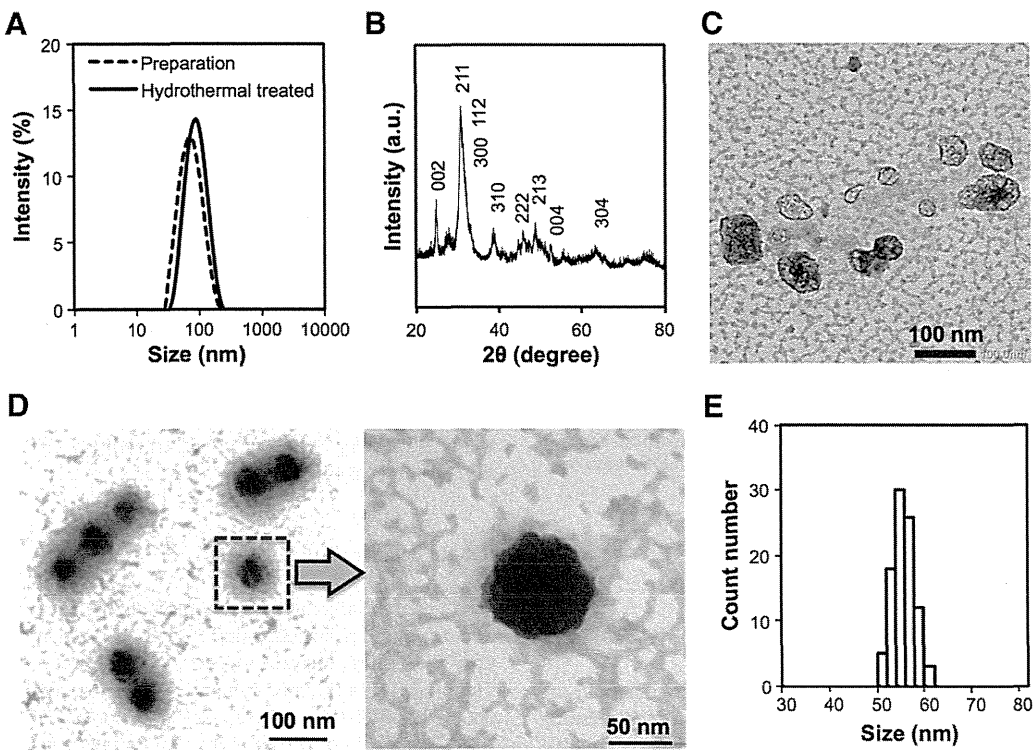

Fig. 2. Characteristics of Gd-DTPA/CaP nanoparticles. (A) DLS-measured z-average diameters of Gd-DTPA/CaP nanoparticles before and after hydrothermal treatment. (B) XRD pattern of Gd-DTPA/CaP nanoparticles, typical peaks of hydroxyapatite ($Ca_{10}(PO_4)_6(OH)_2$) were marked. (C) TEM image of purified Gd-DTPA/CaP nanoparticles without hydrothermal treatments. (D) TEM images of purified Gd-DTPA/CaP nanoparticles with hydrothermal treatments. (E) Number averaged size distribution of Gd-DTPA/CaP nanoparticles calculated from TEM images.

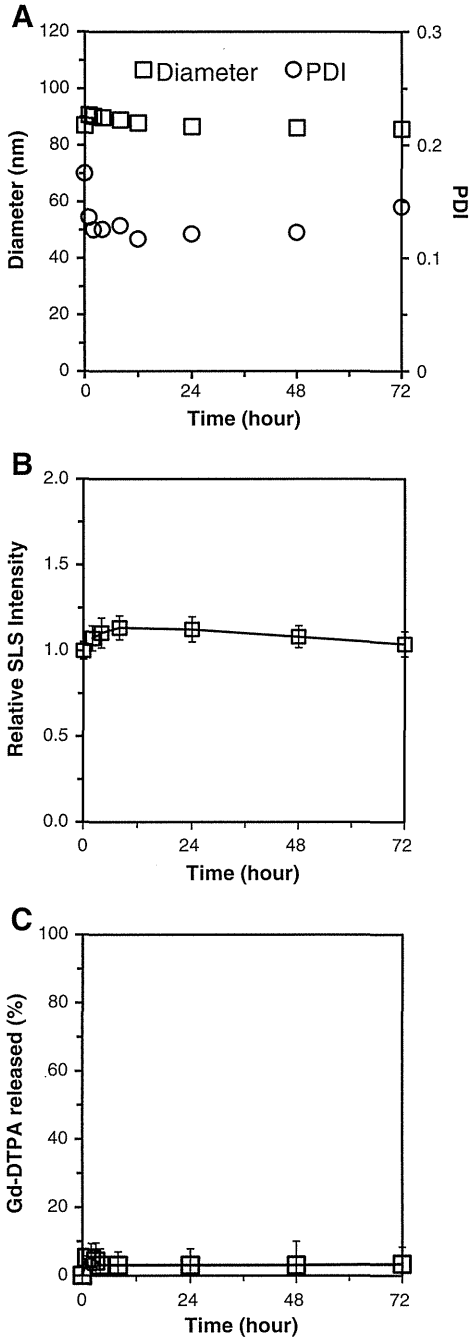

Fig. 3. *In vitro* characterization of Gd-DTPA/CaP nanoparticles in physiological conditions (10 mM PBS buffer, 140 mM NaCl, pH 7.4 and 37 °C). (A) Z-average diameter and PDI changes of Gd-DTPA/CaP determined by DLS. (B) Relative light scattering intensity changes of Gd-DTPA/CaP. (C) Release profiles of Gd-DTPA/CaP.

dramatically increased the stability of these organic–inorganic hybrid CaP nanoparticles in aqueous environments.

3.2. Colloidal stability and Gd-DTPA release profile of Gd-DTPA/CaP

To achieve specific and significant MR contrast enhancement at the tumor site *in vivo*, nanoparticles should be sufficiently stable during circulation in the bloodstream, while minimizing the leakage of contrast agents. Therefore, we evaluated the stability and Gd-DTPA release rate of Gd-DTPA/CaP nanoparticles under physiological conditions. Firstly, the stability of Gd-DTPA/CaP was studied by diluting in 10 mM PBS buffer (140 mM NaCl, pH 7.4) and incubated at 37 °C with continuous shaking. The Z-average diameter and PDI were determined by DLS, while the changes on the light scattering intensity were determined as they reflect the variation in the apparent molecule weight and concentration of nanoparticles. Accordingly, the z-average diameter and PDI of Gd-DTPA/CaP almost did not change at physiological condition (Fig. 3A). Besides, the relative light scattering intensity of Gd-DTPA/CaP nanoparticles increased a little in PBS buffer at initial 24 h and finally decreased slowly (Fig. 3B), this may be caused by interactions of Ca^{2+} with phosphate in PBS buffer. The DLS and SLS results demonstrated that hydrothermal treated Gd-DTPA/CaP nanoparticles were stable in physiological conditions. Moreover, the release profile of Gd-DTPA from Gd-DTPA/CaP in physiological conditions was obtained by measuring the amount of released Gd-DTPA by ICP-MS after dialysis against 10 mM PBS buffer (pH 7.4, NaCl 140 mM) at 37 °C. Thus, Gd-DTPA was slowly released from the nanoparticles, and only 5% of the loaded Gd-DTPA was released in 72 h (Fig. 3C), which was also contributed by the high stability of hydrothermal treated Gd-DTPA/CaP nanoparticles in physiological conditions.

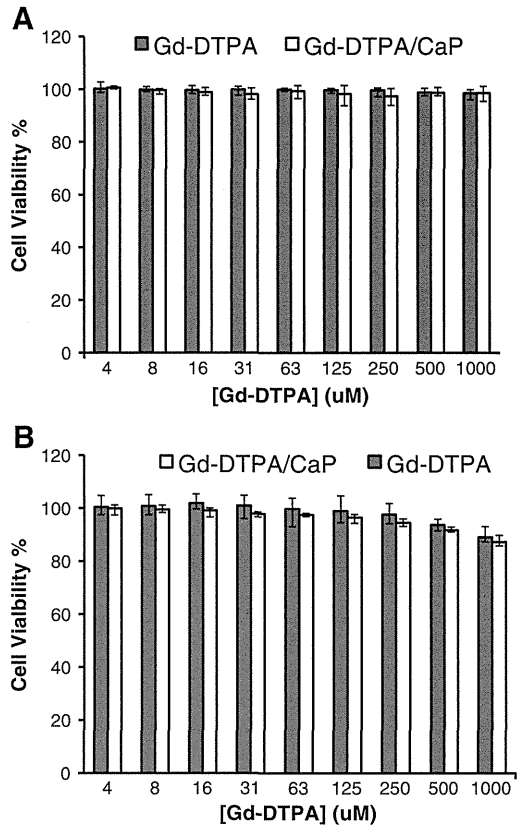

Fig. 4. Cytotoxicity results of Gd-DTPA/CaP against (A) C-26 cells and (B) HUVEC after 72 h incubation.

3.3. Cytotoxicity of Gd-DTPA/CaP

The potential toxicity of nanoparticles is a dominant factor for their applications in clinical imaging. Moreover, rapid increase of intracellular Ca^{2+} over physiological concentration may induce cytotoxicity [32,54]. Therefore, we performed comparative dose–response cytotoxicity studies of Gd-DTPA/CaP and free Gd-DTPA against HUVEC and C-26 cells. After 72 h of exposure, no obvious cytotoxicity was found against both cell lines (Fig. 4). Herein, Gd-DTPA/CaP showed cell viability profiles similar to clinically approved Gd-DTPA, and the low cytotoxicity of Gd-DTPA/CaP benefits its further applications.

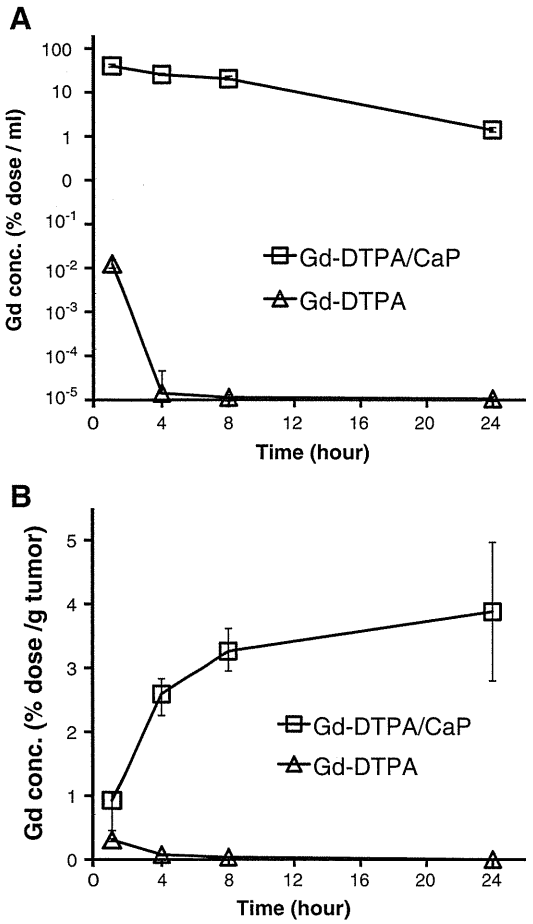

Fig. 5. *In vivo* biodistribution of Gd-DTPA/CaP and Gd-DTPA following tail-vein injection. (A) Log-linear blood circulation profiles of Gd-DTPA/CaP and Gd-DTPA. (B) Tumor accumulation levels of Gd-DTPA/CaP and Gd-DTPA.

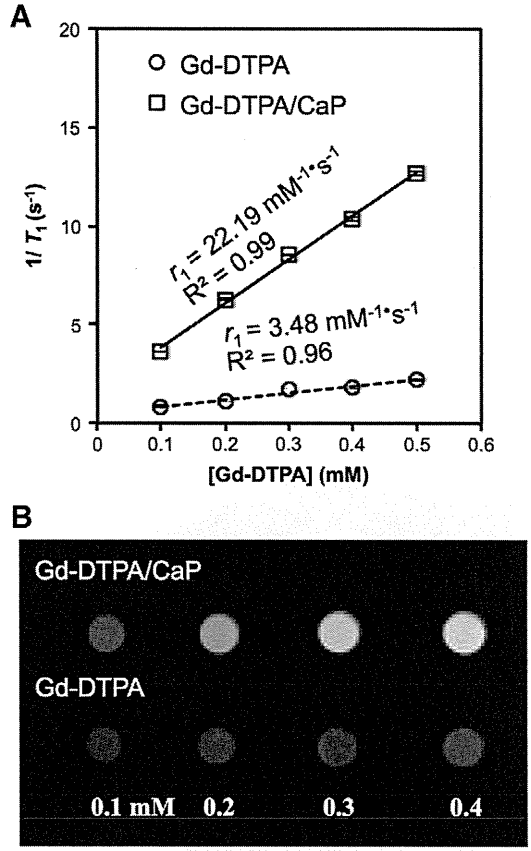

Fig. 7. MR enhancement effects of Gd-DTPA/CaP and Gd-DTPA. (A) T_1 relaxivity coefficients of Gd-DTPA/CaP and Gd-DTPA characterized by ^{1}H-NMR analyzer at 0.59 T. (B) T_1 weight MR images of Gd-DTPA/CaP and free Gd-DTPA solutions at 1 T MRI.

3.4. *In vivo* biodistribution of Gd-DTPA/CaP

Bioavailability and targeting ability of Gd-DTPA/CaP are extremely important for their *in vivo* applications, and can be reflected from plasma clearance and accumulation in tumors. Thus, we measured the amounts of Gd-DTPA delivered by Gd-DTPA/CaP in plasma and in subcutaneous C-26 tumors, and then compared the results with those after administration of free Gd-DTPA. Thus, free Gd-DTPA was rapidly cleared from plasma, and only trace amounts (nearly 0.001% dose/ml) were found in plasma 1 h after intravenous administration (Fig. 5A). Accordingly, Gd-DTPA is a small molecular compound, which could be

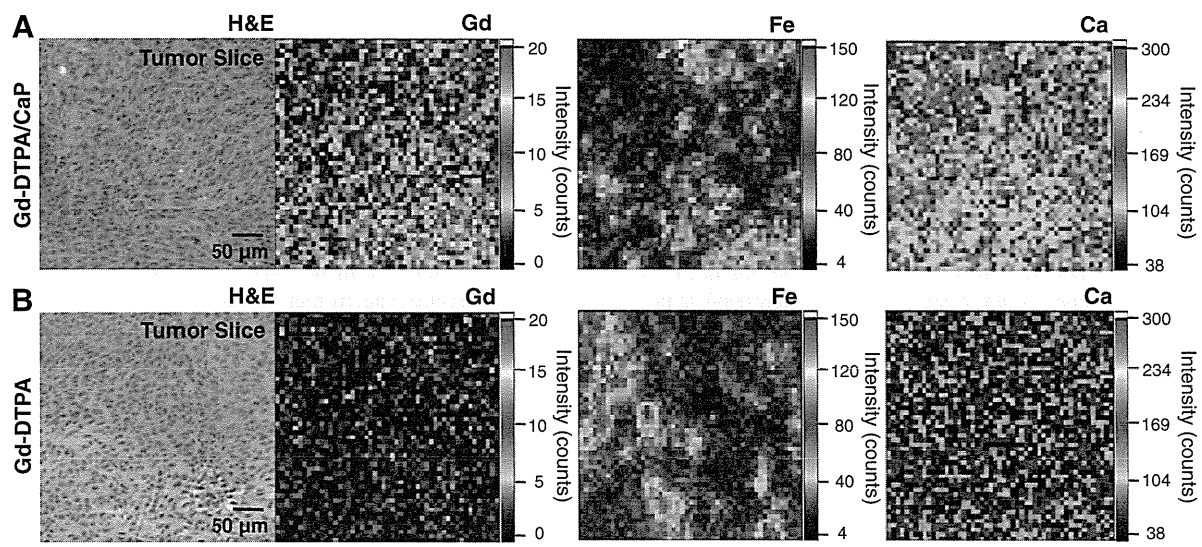

Fig. 6. Micro-distributions of Gd-DTPA/CaP and Gd-DTPA in tumor sections scanned by μ-SR-XRF. (A) H&E staining of tumor section and Gd, Fe and Ca elements distributions in tumor slice 4 h post intravenous injection of Gd-DTPA/CaP. (B) H&E staining of tumor section and Gd, Fe and Ca elements distributions in tumor slice 4 h post intravenous injection of Gd-DTPA.

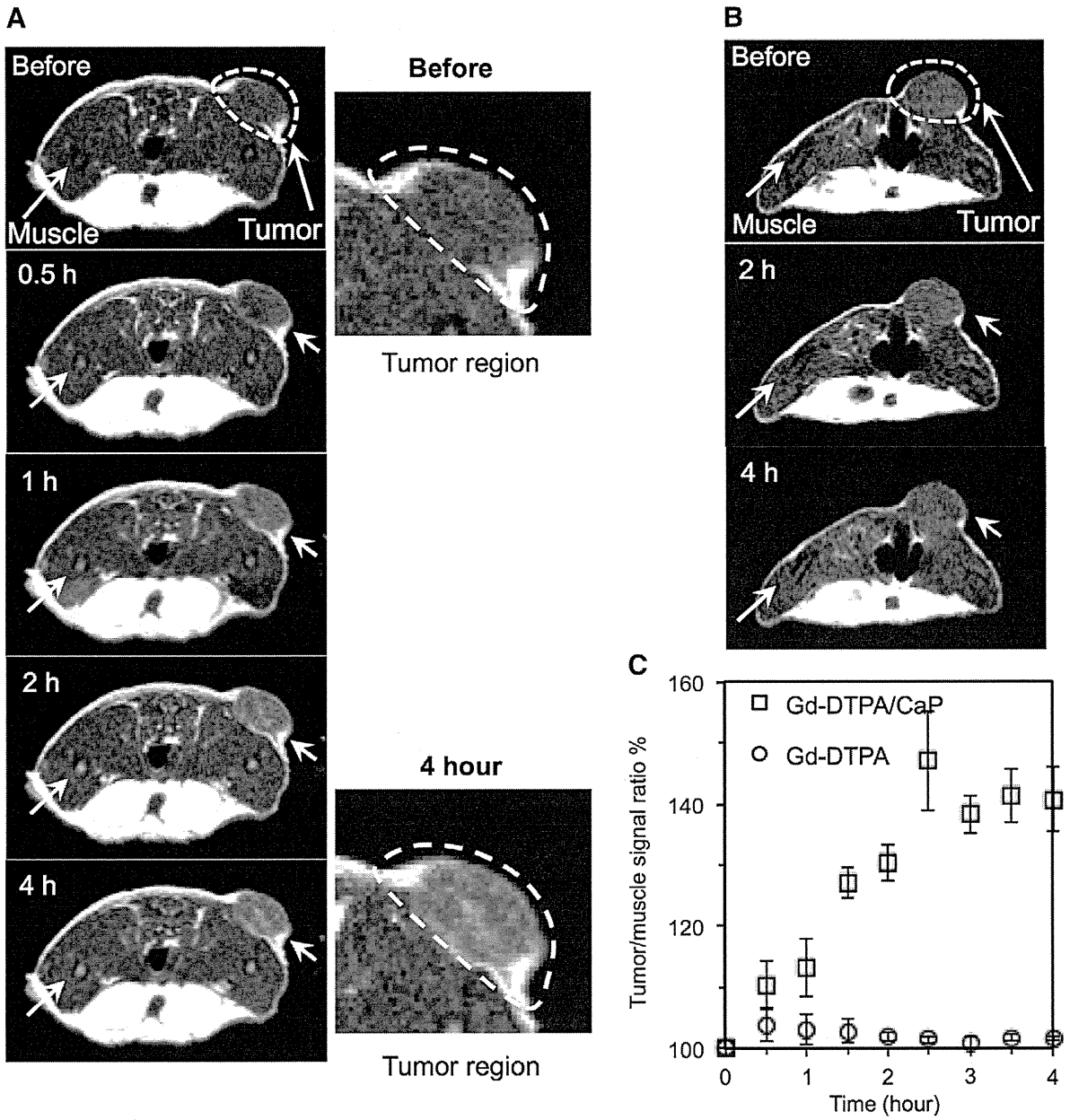

Fig. 8. *In vivo* MRI results of C-26 subcutaneous tumor model bearing Balb/c nude mice following tail-vein injection of Gd-DTPA/CaP and Gd-DTPA as contrast agents. (A) Represent MRI images of C-26 subcutaneous tumor model bearing Balb/c nude mice contrasted by Gd-DTPA/CaP after intravenous injection. (B) Represent MRI images of C-26 subcutaneous tumor model bearing Balb/c nude mice contrasted by Gd-DTPA after intravenous injection. (C) Tumor to muscle signal ratios calculated from MRI images.

easily excreted from blood circulation, and it has been reported that only 10% of injected Gd-DTPA remains in blood after 5 min of administration in rats [48]. Therefore, high doses or multi-injection of Gd (III) chelates is usually applied in clinical settings, but this may result in inaccuracies of diagnosis and potential toxicity [4]. Indeed, free Gd-DTPA did not accumulate in the tumor tissue (Fig. 5B). For Gd-DTPA/CaP, over 40% of Gd-DTPA was found in plasma 1 h after administration, and approximately 20% remained even 8 h later (Fig. 5A), indicating that the blood circulation time of Gd-DTPA was remarkably extended by loading in CaP nanoparticles. Gd-DTPA/CaP gradually accumulated in tumor positions after intravenous injection, to reach nearly 4% of the injected dose per gram tissue after 4 h (Fig. 5B). The accumulation profile may be contributed by the EPR effect observed for macromolecular drug carriers [24].

The extravasation and penetration of nanoparticles in tumors tissues critically affect their contrast enhancing ability, as they will determine the distribution and duration of the MR signal improvements [55]. Thus, we studied the micro-distribution of Gd-DTPA/CaP in the tumors by using micro-synchrotron radiation-induced X-ray fluorescence spectrometry (μ-SR-XRF). μ-SR-XRF is applied to analyze the element distribution of Gd and Ca from Gd-DTPA/CaP in tumor slices [51]. Moreover, Fe atoms from hemeproteins were detected to infer the presence of blood vessels. Accordingly, μ-SR-XRF was used to detect tumor slices harvested 4 h after administration of Gd-DTPA/CaP or free Gd-DTPA. As shown in Fig. 6, higher intensity of Ca and Gd was found in tumor slices administrated with Gd-DTPA/CaP than control Gd-DTPA, revealing the enhanced accumulation of Gd-DTPA/CaP. Moreover, the presence of the Gd and Ca atoms for Gd-DTPA/CaP was homogeneous and distant from the Fe-rich areas of blood vessels, suggesting deep tumor penetration of the Gd-DTPA/CaP nanoparticles.

3.5. MRI contrast enhancing ability of Gd-DTPA/CaP

For MRI probes, molecular relaxivity is an important parameter, which determines the contrast ability of a paramagnetic compound, as higher molecular relaxivity (r_1) contributes to higher signal enhancement. To evaluate the molecular relaxivity of Gd-DTPA loaded Gd-DTPA/CaP, we used a 0.59 T pulse-NMR. Thus, r_1 value of Gd-DTPA in Gd-DTPA/CaP increased nearly 6 times from 3.48 mM^{-1} s^{-1} of free Gd-DTPA to 22.19 mM^{-1} s^{-1} (Fig. 7A). The relaxivity of Gd^{3+} ions from $GdCl_3$ in aqueous solution was 10.61 mM^{-1} s^{-1}, which is lower than Gd-DTPA/CaP. Meanwhile, the r_1 of Gd-DTPA released from Gd-DTPA/CaP by dialysis of Gd-DTPA/CaP in Mili-Q water was 3.34 mM^{-1} s^{-1} (Fig. S1), which is similar to that of Gd-DTPA, suggesting there was no free Gd^{3+} ion in Gd-DTPA/CaP nanoparticles. In addition, 1 T MRI results confirmed that Gd-DTPA/CaP has higher contrast ability than Gd-DTPA, as the images of Gd-DTPA/CaP were much whiter than free Gd-DTPA at the same concentration (Fig. 7B). The high molecular relaxivity of Gd-DTPA/CaP may result from both the additive effect of all of the Gd^{3+} paramagnetic centers and the reduction of molecular tumbling rates, which increases the r_1 value of each Gd-chelate in the confined space of CaP [17–19,21,26].

Finally, Gd-DTPA/CaP and Gd-DTPA were used to enhance the MR contrast of C-26 subcutaneous tumors *in vivo* (Fig. 8A and B). After intravenous injection of Gd-DTPA/CaP, the contrast of the tumor position was gradually enhanced, reaching more than 40% increase in the signal ratio of the tumor to the muscle at 4 h-post administration (Fig. 8C). The higher contrast of tumor positions by Gd-DTPA/CaP might result from both the promoted accumulation of Gd-DTPA and the increased molecular relaxivity of Gd-DTPA inside Gd-DTPA/CaP. By incorporation of Gd-DTPA inside sub-100 nm CaP nanoparticles, higher amounts of contrast agent were selectively delivered to tumor positions by EPR effect (Fig. 5), increasing the contrast with the surrounding tissues. Meanwhile, as Gd-DTPA/CaP exhibited higher molecular relaxivity than free Gd-DTPA, the contrast in tumor positions was enhanced more efficiently than the conventional contrast agent. Thus, no signal enhancement was observed for free Gd-DTPA even administrated with 4 times higher dose than that of Gd-DTPA/CaP. These results demonstrated that MRI contrast enhancing ability of Gd-DTPA was greatly improved by incorporation into CaP nanoparticles.

4. Conclusion

In this study, Gd-DTPA/CaP nanoparticles with unique colloidal stability, biodegradation and magnetic properties were synthesized by following a facile two-step preparation approach, and used for MRI contrast enhancement of solid tumors. Thus, as all of the components are non-toxic and biocompatible materials, Gd-DTPA/CaP is expected to become an important candidate for diagnosis of malignant tumors. Moreover, the two-step preparation method of Gd-DTPA/CaP represents a facile and promising strategy for incorporating bioactive molecules in CaP nanoparticles for the construction of safe and efficient drug carriers for biomedical applications. The hydrothermal treatment procedure significantly enhanced the colloidal stability of CaP nanoparticles and the relaxivity of Gd-DTPA was enhanced after loading in the CaP matrix. This strategy may be utilized to develop other CaP-based drug delivery systems, and further applied for developing other inorganic-materials based nanocarriers.

Acknowledgments

This research was financially supported by Funding Program for World-Leading Innovative R&D on Science and Technology (FIRST) from the Japan Society for the Promotion of Science (JSPS) (K.K.) and Takeda Science Foundation (N.N.). P.M. thanks the support of a JSPS fellowship. TEM measurements were conducted in Research Hub for Advanced Nano Characterization, The University of Tokyo, supported by the Ministry of Education, Culture, Sports, Science and Technology (MEXT), Japan. μ-SR-XRF characterizations were supported by the Nanotechnology Support Program of the Japan Synchrotron Radiation Research Institute (JASRI). We thank Ms. Sayaka Shibata and Ms. Aiko Sekita (NIRS) for technical support.

Appendix A. Supplementary data

Supplementary data to this article can be found online at http://dx.doi.org/10.1016/j.jconrel.2013.10.038.

References

[1] M.G. Harisinghani, J. Barentsz, P.F. Hahn, W.M. Deserno, S. Tabatabaei, C.H. van de Kaa, J. de la Rosette, R. Weissleder, Noninvasive detection of clinically occult lymph-node metastases in prostate cancer, N. Engl. J. Med. 348 (2003) 2491–2499.
[2] H.B. Na, T. Hyeon, Nanostructured T1 MRI contrast agents, J. Mater. Chem. 19 (2009) 6267–6273.
[3] P. Caravan, J.J. Ellison, T.J. McMurry, R.B. Lauffer, Gadolinium (III) chelates as MRI contrast agents: structure, dynamics, and applications, Chem. Rev. 99 (1999) 2293–2352.
[4] M.F. Kircher, A. de la Zerda, J.V. Jokerst, C.L. Zavaleta, P.J. Kempen, E. Mittra, K. Pitter, R.M. Huang, C. Campos, F. Habte, R. Sinclair, C.W. Brennan, I.K. Mellinghoff, E.C. Holland, S.S. Gambhir, A brain tumor molecular imaging strategy using a new triple-modality MRI-photoacoustic-raman nanoparticle, Nat. Med. 18 (2012) 829–834.
[5] N. Nasongkla, E. Bey, J.M. Ren, H. Ai, C. Khemtong, J.S. Guthi, S.F. Chin, A.D. Sherry, D.A. Boothman, J.M. Gao, Multifunctional polymeric micelles as cancer-targeted, MRI-ultrasensitive drug delivery systems, Nano Lett. 6 (2006) 2427–2430.
[6] P. Mi, H. Cabral, D. Kokuryo, M. Rafi, Y. Terada, I. Aoki, T. Saga, T. Ishii, N. Nishiyama, K. Kataoka, Gd-DTPA-loaded polymer-metal complex micelles with high relaxivity for MR cancer imaging, Biomaterials 34 (2013) 492–500.
[7] S. Kaida, H. Cabral, M. Kumagai, A. Kishimura, Y. Terada, M. Sekino, I. Aoki, N. Nishiyama, T. Tani, K. Kataoka, Visible drug delivery by supramolecular nanocarriers directing to single-platformed diagnosis and therapy of pancreatic tumor model, Cancer Res. 70 (2010) 7031–7041.
[8] J. Lu, S.L. Ma, J.Y. Sun, C.C. Xia, C. Liu, Z.Y. Wang, X.N. Zhao, F.B. Gao, Q.Y. Gong, B. Song, X.T. Shuai, H. Ai, Z.W. Gu, Manganese ferrite nanoparticle micellar nanocomposites as MRI contrast agent for liver imaging, Biomaterials 30 (2009) 2919–2928.
[9] H. Ai, C. Flask, B. Weinberg, X. Shuai, M.D. Pagel, D. Farrell, J. Duerk, J.M. Gao, Magnetite-loaded polymeric micelles as ultrasensitive magnetic-resonance probes, Adv. Mater. 17 (2005) 1949–1952.
[10] E. Nakamura, K. Makino, T. Okano, T. Yamamoto, M. Yokoyama, A polymeric micelle MRI contrast agent with changeable relaxivity, J. Control. Release 114 (2006) 325–333.
[11] G. Mikhaylov, U. Mikac, A.A. Magaeva, V.I. Itin, E.P. Naiden, I. Psakhye, L. Babes, T. Reinheckel, C. Peters, R. Zeiser, M. Bogyo, V. Turk, S.G. Psakhye, B. Turk, O. Vasiljeva, Ferri-liposomes as an MRI-visible drug-delivery system for targeting tumours and their microenvironment, Nat. Nanotechnol. 6 (2011) 594–602.
[12] Z.Y. Liao, H.J. Wang, X.D. Wang, P.Q. Zhao, S. Wang, W.Y. Su, J. Chang, Multifunctional nanoparticles composed of a poly(DL-lactide-coglycolide) core and a paramagnetic liposome shell for simultaneous magnetic resonance imaging and targeted therapeutics, Adv. Funct. Mater. 21 (2011) 1179–1186.
[13] H. Grull, S. Langereis, L. Messager, D.D. Castelli, A. Sanino, E. Torres, E. Terreno, S. Aime, Block copolymer vesicles containing paramagnetic lanthanide complexes: a novel class of T-1- and CEST MRI contrast agents, Soft Matter 6 (2010) 4847–4850.
[14] D. Kokuryo, Y. Anraku, A. Kishimura, S. Tanaka, M.R. Kano, J. Kershaw, N. Nishiyama, T. Saga, I. Aoki, K. Kataoka, SPIO-PICsome: development of a highly sensitive and stealth-capable MRI nano-agent for tumor detection using SPIO-loaded unilamellar polyion complex vesicles (PICsomes), J. Control. Release 169 (2013) 220–227.
[15] H.Y. Lee, Z. Li, K. Chen, A.R. Hsu, C.J. Xu, J. Xie, S.H. Sun, X.Y. Chen, PET/MRI dual-modality tumor imaging using arginine-glycine-aspartic (RGD)-conjugated radiolabeled iron oxide nanoparticles, J. Nucl. Med. 49 (2008) 1371–1379.
[16] M. Kumagai, M.R. Kano, Y. Morishita, M. Ota, Y. Imai, N. Nishiyama, M. Sekino, S. Ueno, K. Miyazono, K. Kataoka, Enhanced magnetic resonance imaging of experimental pancreatic tumor *in vivo* by block copolymer-coated magnetite nanoparticles with TGF-beta inhibitor, J. Control. Release 140 (2009) 306–311.
[17] E. Vucic, H.M. Sanders, F. Arena, E. Terreno, S. Aime, K. Nicolay, E. Leupold, M. Dathe, N.A. Sommerdijk, Z.A. Fayad, W.J.M. Mulder, Well-defined, multifunctional nanostructures of a paramagnetic lipid and a lipopeptide for macrophage imaging, J. Am. Chem. Soc. 131 (2009) 406–407.
[18] W.J.M. Mulder, G.J. Strijkers, G.A.F. van Tilborg, A.W. Griffioen, K. Nicolay, Lipid-based nanoparticles for contrast-enhanced MRI and molecular imaging, NMR Biomed. 19 (2006) 142–164.
[19] F. Kielar, L. Tei, E. Terreno, M. Botta, Large relaxivity enhancement of paramagnetic lipid nanoparticles by restricting the local motions of the Gd-III chelates, J. Am. Chem. Soc. 132 (2010) 7836–7837.
[20] G.L. Liang, J. Ronald, Y.X. Chen, D.J. Ye, P. Pandit, M.L. Ma, B. Rutt, J.H. Rao, Controlled self-assembling of gadolinium nanoparticles as smart molecular magnetic resonance imaging contrast agents, Angew. Chem. Int. Ed. 50 (2011) 6283–6286.

[21] A.K. Duncan, P.J. Klemm, K.N. Raymond, C.C. Landry, Silica microparticles as a solid support for gadolinium phosphonate magnetic resonance imaging contrast agents, J. Am. Chem. Soc. 134 (2012) 8046–8049.
[22] M.F. Bennewitz, T.L. Lobo, M.K. Nkansah, G. Ulas, G.W. Brudvig, E.M. Shapiro, Biocompatible and pH-sensitive PLGA encapsulated MnO nanocrystals for molecular and cellular MRI, ACS Nano 5 (2011) 3438–3446.
[23] L.M. Manus, D.J. Mastarone, E.A. Waters, X.Q. Zhang, E.A. Schultz-Sikma, K.W. MacRenaris, D. Ho, T.J. Meade, Gd(III)-nanodiamond conjugates for MRI contrast enhancement, Nano Lett. 10 (2010) 484–489.
[24] Y. Matsumura, H. Maeda, A new concept for macromolecular therapeutics in cancer chemotherapy: mechanism of tumoritropic accumulation of proteins and the antitumor agent smancs, Cancer Res. 46 (1986) 6387–6392.
[25] P. Caravan, C.T. Farrar, L. Frullano, R. Uppal, Influence of molecular parameters and increasing magnetic field strength on relaxivity of gadolinium- and manganese-based T_1 contrast agents, Contrast Media Mol. Imaging 4 (2009) 89–100.
[26] J.S. Ananta, B. Godin, R. Sethi, L. Moriggi, X.W. Liu, R.E. Serda, R. Krishnamurthy, R. Muthupillai, R.D. Bolskar, L. Helm, M. Ferrari, L.J. Wilson, P. Decuzzi, Geometrical confinement of gadolinium-based contrast agents in nanoporous particles enhances T_1 contrast, Nat. Nanotechnol. 5 (2010) 815–821.
[27] M. Liong, J. Lu, M. Kovochich, T. Xia, S.G. Ruehm, A.E. Nel, F. Tamanoi, J.I. Zink, Multifunctional inorganic nanoparticles for imaging, targeting, and drug delivery, ACS Nano 2 (2008) 889–896.
[28] H. Cabral, N. Nishiyama, K. Kataoka, Supramolecular nanodevices: from design validation to theranostic nanomedicine, Acc. Chem. Res. 44 (2011) 999–1008.
[29] A. Jemal, F. Bray, M.M. Center, J. Ferlay, E. Ward, D. Forman, Global cancer statistics, CA Cancer J. Clin. 61 (2011) 69–90.
[30] F.L. Graham, A.J. van der Eb, A new technique for the assay of infectivity of human adenovirus 5 DNA, Virology 52 (1973) 456–467.
[31] M. Epple, K. Ganesan, R. Heumann, J. Klesing, A. Kovtun, S. Neumann, V. Sokolova, Application of calcium phosphate nanoparticles in biomedicine, J. Mater. Chem. 20 (2010) 18–23.
[32] A. Tabakovic, M. Kester, J.H. Adair, Calcium phosphate-based composite nanoparticles in bioimaging and therapeutic delivery applications, Wiley Interdiscip. Rev. Nanomedicine Nanobiotechnol 4 (2012) 96–112.
[33] M.Z. Zhang, K. Kataoka, Nano-structured composites based on calcium phosphate for cellular delivery of therapeutic and diagnostic agents, Nano Today 4 (2009) 508–517.
[34] R.Z. LeGeros, Biodegradation and bioresorption of calcium phosphate ceramics, Clin. Mater. 14 (1993) 65–88.
[35] E.I. Altinoglu, T.J. Russin, J.M. Kaiser, B.M. Barth, P.C. Eklund, M. Kester, J.H. Adair, Near-infrared emitting fluorophore-doped calcium phosphate nanoparticles for in vivo imaging of human breast cancer, ACS Nano 2 (2008) 2075–2084.
[36] J. Li, Y.C. Chen, Y.C. Tseng, S. Mozumdar, L. Huang, Biodegradable calcium phosphate nanoparticle with lipid coating for systemic siRNA delivery, J. Control. Release 142 (2010) 416–421.
[37] V.V. Sokolova, I. Radtke, R. Heumann, M. Epple, Effective transfection of cells with multi-shell calcium phosphate-DNA nanoparticles, Biomaterials 27 (2006) 3147–3153.
[38] V.V. Sokolova, T. Knuschke, A. Kovtun, J. Buer, M. Epple, A.M. Westendorf, The use of calcium phosphate nanoparticles encapsulating toll-like receptor ligands and the antigen hemagglutinin to induce dendritic cell maturation and T cell activation, Biomaterials 31 (2010) 5627–5633.
[39] A.H. Faraji, P. Wipf, Nanoparticles in cellular drug delivery, Bioorg. Med. Chem. 17 (2009) 2950–2962.
[40] G.K. Lim, J. Wang, S.C. Ng, L.M. Gan, Formation of nanocrystalline hydroxyapatite in nonionic surfactant emulsions, Langmuir 15 (1999) 7472–7477.
[41] Y. Kakizawa, K. Kataoka, Block copolymer self-assembly into monodispersive nanoparticles with hybrid core of antisense DNA and calcium phosphate, Langmuir 18 (2002) 4539–4543.
[42] F. Pittella, M.Z. Zhang, Y. Lee, H.J. Kim, T. Tockary, K. Osada, T. Ishii, K. Miyata, N. Nishiyama, K. Kataoka, Enhanced endosomal escape of siRNA-incorporating hybrid nanoparticles from calcium phosphate and PEG-block charge-conversional polymer for efficient gene knockdown with negligible cytotoxicity, Biomaterials 32 (2011) 3106–3114.
[43] Y. Kakizawa, K. Miyata, S. Furukawa, K. Kataoka, Size-controlled formation of a calcium phosphate-based organic–inorganic hybrid vector for gene delivery using poly(ethylene glycol)-*block*-poly(aspartic acid), Adv. Mater. 16 (2004) 699–702.
[44] Y. Kakizawa, S. Furukawa, A. Ishii, K. Kataoka, Organic–inorganic hybrid-nanocarrier of siRNA constructing through the self-assembly of calcium phosphate and PEG-based block aniomer, J. Control. Release 111 (2006) 368–370.
[45] Y. Kakizawa, S. Furukawa, K. Kataoka, Block copolymer-coated calcium phosphate nanoparticles sensing intracellular environment for oligodeoxynucleotide and siRNA delivery, J. Control. Release 97 (2004) 345–356.
[46] F. Pittella, K. Miyata, Y. Maeda, T. Suma, S. Watanabe, Q. Chen, R.J. Christie, K. Osada, N. Nishiyama, K. Kataoka, Pancreatic cancer therapy by systemic administration of VEGF siRNA contained in calcium phosphate/charge-conversional polymer hybrid nanoparticles, J. Control. Release 161 (2012) 868–874.
[47] M. Zhang, A. Ishii, N. Nishiyama, S. Matsumoto, T. Ishii, Y. Yamasaki, K. Kataoka, PEGylated calcium phosphate nanocomposites as smart environment-sensitive carriers for siRNA delivery, Adv. Mater. 21 (2009) 1–6.
[48] H.J. Weinmann, R.C. Brasch, W.R. Press, G.E. Wesbey, Characteristics of gadolinium-DTPA complex: a potential NMR contrast agent, AJR Am. J. Roentgenol. 142 (1984) 619–624.
[49] Y.J. Wang, S.H. Zhang, K. Wei, N.R. Zhao, J.D. Chen, X.D. Wang, Hydrothermal synthesis of hydroxyapatite nanopowders using cationic surfactant as a template, Mater. Lett. 60 (2006) 1484–1487.
[50] A. Koide, A. Kishimura, K. Osada, W.D. Jang, Y. Yamasaki, K. Kataoka, Semipermeable polymer vesicle (PICsome) self-assembled in aqueous medium from a pair of oppositely charged block copolymers: physiologically stable micro-/nanocontainers of water-soluble macromolecules, J. Am. Chem. Soc. 128 (2006) 5988–5989.
[51] Y. Terada, S. Goto, N. Takimoto, K. Takeshita, H. Yamazaki, Y. Shimizu, S. Takahashi, H. Ohashi, Y. Furukawa, T. Matsushita, T. Ohata, Y. Ishizawa, T. Uruga, H. Kitamura, T. Ishikawa, S. Hayakawa, Construction and commissioning of BL37XU at SPring-8, AIP Conf. Proc. 705 (2004) 376–379.
[52] L. Yan, Y.D. Li, Z.X. Deng, J. Zhuang, X.M. Sun, Surfactant-assisted hydrothermal synthesis of hydroxyapatite nanorods, Int. J. Inorg. Mater. 3 (2001) 633–637.
[53] A.A. Chaudhry, S. Haque, S. Kellici, P. Boldrin, I. Rehman, A.K. Fazal, J.A. Darr, Instant nano-hydroxyapatite: a continuous and rapid hydrothermal synthesis, Chem. Commun. 21 (2006) 2286–2288.
[54] C. Cerella, M. Diederich, L. Ghibelli, The dual role of calcium as messenger and stressor in cell damage, death, and survival, Int. J. Cell Biol. 2010 (2010) 1–14.
[55] A.I. Minchinton, I.F. Tannock, Drug penetration in solid tumours, Nat. Rev. Cancer 6 (2006) 583–592.

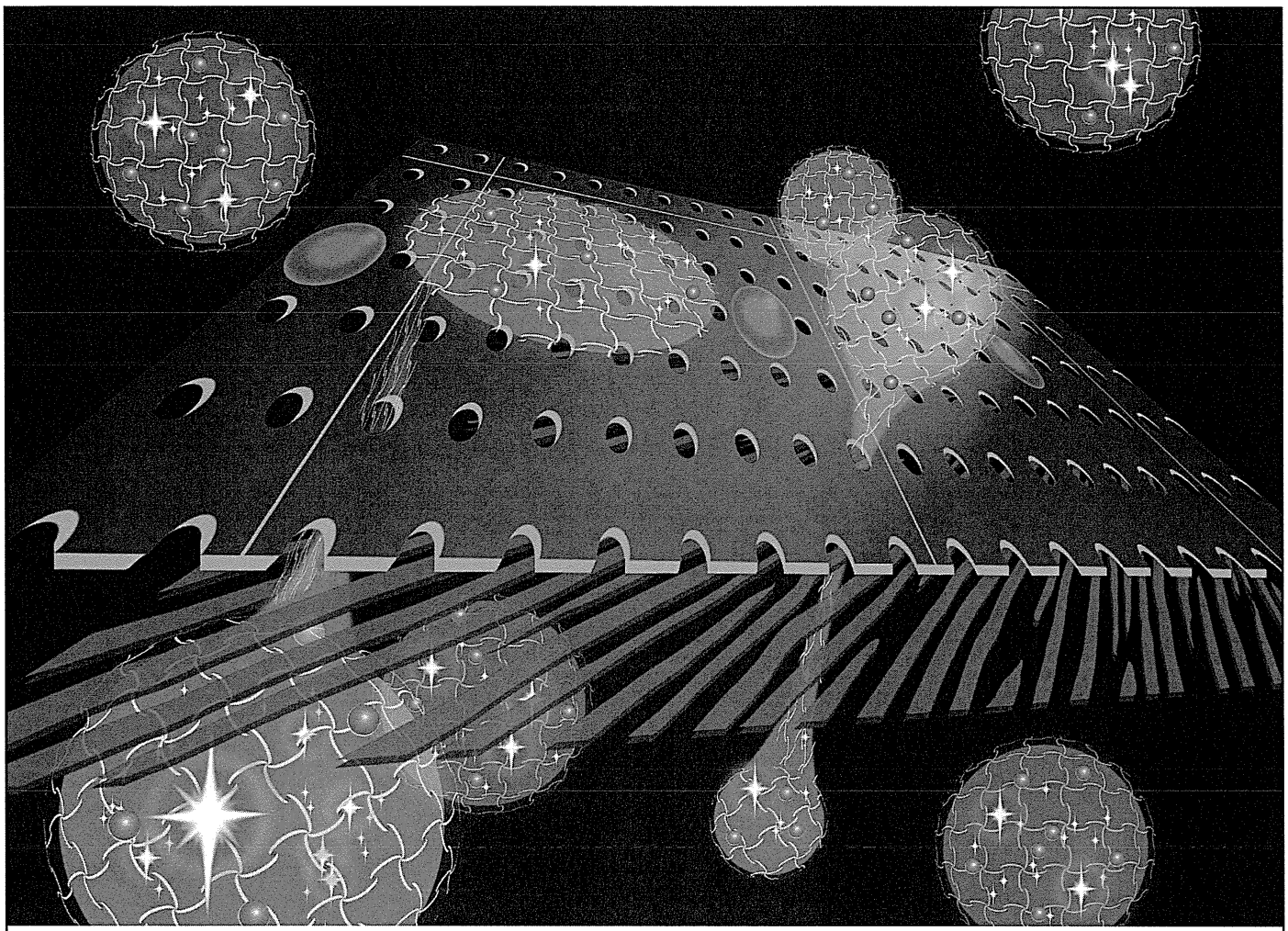

Showcasing collaborative research from the Masaru Kato lab (Graduate School of Pharmaceutical Sciences and GPLLI Program, The University of Tokyo, Tokyo, Japan), and the Ichio Aoki lab (Molecular Imaging Center, National Institute of Radiological Sciences, Chiba, Japan).

Title: The simple preparation of polyethylene glycol-based soft nanoparticles containing dual imaging probes

The PEG-based nanoparticles that encapsulate dual imaging probes were soft and excreted by the mice rapidly through urine. The PEG-based soft nanoparticles will be a safer carrier for diagnostic agents.

As featured in:

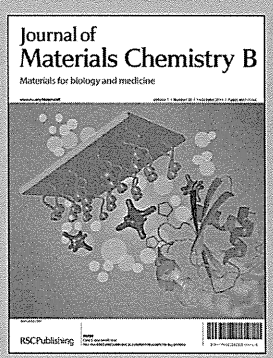

See S. Murayama *et al.*,
J. Mater. Chem. B, 2013, **1**, 4932.

RSC Publishing

www.rsc.org/MaterialsB

Registered Charity Number 207890

Journal of Materials Chemistry B

RSC Publishing

PAPER

View Article Online
View Journal | View Issue

The simple preparation of polyethylene glycol-based soft nanoparticles containing dual imaging probes†

Cite this: *J. Mater. Chem. B*, 2013, **1**, 4932

Shuhei Murayama,[ab] Jun-ichiro Jo,[b] Yuka Shibata,[a] Kun Liang,[c] Tomofumi Santa,[a] Tsuneo Saga,[b] Ichio Aoki[b] and Masaru Kato*[a]

Received 10th June 2013
Accepted 30th July 2013

DOI: 10.1039/c3tb20828a

www.rsc.org/MaterialsB

We developed a simple method to prepare PEG-based soft nanoparticles that encapsulate dual imaging probes. Because the probes could be encapsulated by either chemical or physical means, a variety of probe molecules were encapsulated within the nanoparticles simultaneously. The nanoparticles were administrated to mice and the pharmacokinetics of the nanoparticles was analyzed by means of MRI, fluorescence spectroscopy, and transmission electron microscopy. The soft nanoparticles were excreted by the mice rapidly through the urine without collapse of the nanoparticles and without leaking of the probe molecules, and no accumulation of the nanoparticles in the body was observed. The pharmacokinetics of the nanoparticles was not changed by the encapsulated molecules and acute toxicity to mice was negligible. It was expect that these PEG-based soft nanoparticles will be applicable for use as a safe diagnostic agent.

Introduction

Dual or multi-probe molecules, which are composed of combinations of two or more functional molecules, are attractive for use as tools for noninvasive diagnosis and therapy.[1–4] Such dual and multi-probes improve the reliability and safety of the diagnoses as they mutually complement one another.

Although many dual or multi-probes have been reported, most of these probes have been designed by bonding two different probe molecules directly or indirectly with the aid of a linker molecule.[1–6] For the linkage of two different probe molecules, the probe molecules must have appropriate functional groups for linkages and must also retain their functionality after being linked. Nanoparticles are promising materials for dual or multi-probe preparation because in addition to bonding, encapsulation and adsorption they are available for the immobilization of probe molecules to the nanoparticles.[7–12] In general, small nanoparticles show low potential toxicity risk, because they are rapidly excreted through the urine and they are suitable for clinical applications. However, the sensitivity of them is low, because of their small volume. For this reason, large nanoparticles that are excreted through the urine are ideal materials in terms of safety and detection.

We have developed a method for preparing polyethylene glycol (PEG)-based nanoparticles that contain various kinds of probe molecules, as reported previously.[13,14] The nanoparticles were prepared from monomer molecules that consisted of four long PEG chains with acryloyl groups at each chain end. Simply adding the probe molecules to a solution of the monomers resulted in the formation of uniformly sized nanoparticles that encapsulated the probe molecules. Because the encapsulated molecules are physically trapped by the mesh structure of the nanoparticles and because no chemical bonding between the molecules and PEG is required for encapsulation,[15,16] we concluded that there are no limitations to the types of molecules that can be encapsulated using this technique. Only two acryloyl groups were required to form a mesh structure for physical encapsulation of molecules within the nanoparticles, and thus we expected that the one of the two remaining acryloyl groups on each monomer could be used for chemical reactions with the probe molecules. To test this hypothesis, we encapsulated probe molecules in the PEG-based nanoparticles, by chemical means, in addition to the physical encapsulation. We speculated that if we encapsulated two different probes using two different (*i.e.*, chemical and physical) methods simultaneously, a dual probe could be prepared without limitation of the encapsulated molecules. In this study, we prepared three different dual probe nanoparticles containing physically and chemically encapsulated probe molecules. The physical properties of these nanoparticles were examined, and the nanoparticles were used for animal experiments to examine their pharmacokinetics and toxicity.

[a]*Graduate School of Pharmaceutical Sciences and GPLLI Program The University of Tokyo, 7-3-1 Hongo, Bunkyo-ku, Tokyo 113-0033, Japan. E-mail: masaru-kato@umin.ac.jp*

[b]*Molecular Imaging Center, National Institute of Radiological Sciences, 4-9-1 Anagawa, Inage-ku, Chiba 263-8555, Japan*

[c]*Center for Medical Systems Innovation Summer Internship Program, The University of Tokyo, Japan*

† Electronic supplementary information (ESI) available. See DOI: 10.1039/c3tb20828a

Experimental section

Materials

Tetra-poly(ethyl glycol)-amine (SUNBRIGHT PTE-050PA; M_n, 5328 g mol^{-1}) was purchased from NOF Corporation (Tokyo, Japan). *N*,*N*,*N*′,*N*′-Tetramethylethylenediamine (TEMED), triethylamine (TEA), acryloyl chloride (AC), dichloromethane (DCM), ammonium persulfate (APS), tris(hydroxymethyl) aminomethane (Tris), hydrochloric acid, methanol, diethyl ether, acetic acid, magnesium sulfate, fluorescein (Flu), and 4-(4,6-dimethoxy-1,3,5-triazin-2-yl)-4-methylmorpholinium chloride *n*-hydrate (DMT-MM) were purchased from Wako Pure Chemical Industries (Osaka, Japan). Dextran with a weight-averaged molecular weight of 40 000 (Dex), diethylenetriaminepentaacetic acid (DTPA) anhydride, manganese chloride, ferritin type I from horse spleen, and fluorescein isothiocyanate–dextran, molecular weight of 40 000 (Dex–Flu) was purchased from Sigma-Aldrich (St. Louis, MO). Alexa Fluor 647 carboxylic acid, succinimidyl ester was purchased from Invitrogen Corporation (Carlsbad, CA). Dimethyl sulfoxide (DMSO), 2-morpholineoethanesulfonic acid and 4-dimethylaminopyridine (DMAP) were obtained from Nacalai Tesque. Inc. (Kyoto, Japan). 2-Hydroxyethyl acrylate (AC-OH) was purchased from Tokyo Chemical Industry Co., LTD. (Tokyo, Japan). Water was purified with a Milli-Q apparatus (Millipore, Bedford, MA).

Preparation of Dex-Mn

DTPA anhydride (920 μmol) and DMAP (130 μmol) were added to 10 mL of dehydrated dimethyl sulfoxide containing 100 mg (1.9 mmol of hydroxyl (OH) groups) of dextran. The reaction solution was agitated at room temperature for 18 h to introduce DTPA residues to the OH of dextran, followed by dialysis against double distilled water for 2 days and freeze-drying to obtain DTPA-introduced dextran (Dex-DTPA). The extent of DTPA residues introduced to dextran OH groups was measured by conventional conductometric titration and calculated to be 10.2%. To 1 mL of Dex-DTPA solution (10 mg mL^{-1}, 19 μmol DTPA), 0.2 mL of manganese chloride solution (94 mg mL^{-1}, 95 μmol) was added in 0.1 M 2-morpholineoethanesulfate (MES)-buffered solution (pH 6.0). The mixtures were agitated at room temperature for 3 h to chelate Mn^{2+} to the DTPA residues. The reaction solution was purified by a PD-10 column (GE healthcare UK Ltd., Buckinghamshire, UK) with water and freeze-drying to obtain Mn^{2+}-chelated Dex-DTPA (Dex-Mn). The extent of Mn^{2+} chelated to DTPA residues was measured by atomic absorption spectrophotometer (AA-6800, Shimadzu Corp., Kyoto, Japan) and calculated to be 75%.

Preparation of short wave fluorescence linker (PEG-Flu-3AC)

Tetra-poly(ethyl glycol)-amine (2) (120 μmol) and Flu (1) (120 μmol) were dissolved in methanol and stirred until all reactants were dissolved in a lightproof vial. After that, DMT-MM (300 μmol) was added to start the synthesis without stirring. The reaction was done at room temperature for 3 h. The product was precipitated in diethyl ether on ice and filtered. The collected substance was washed with diethyl ether and dissolved in water. The aqueous solution was evaporated, dialyzed (SpectraPor6, CO 1000 g mol^{-1}) and freeze-dried to yield a fluorescent product (PEG-Flu-3NH (3)). PEG-Flu-3NH (18 μmol) was dissolved in dry DCM and stirred in a lightproof vial purged with N_2 gas. TEA (71 μmol) and excess amount of AC (177 μmol) were added dropwise on ice and stirred 3 h. After the reaction, the product was resolved in methanol, precipitated in diethyl ether on ice and filtered. The collected substance was washed with diethyl ether and dissolved in water. The aqueous solution was evaporated, dialyzed (SpectraPor6, CO 1000 g mol^{-1}) and freeze-dried to yield a fluorescent product (PEG-Flu-3AC (4)) (Scheme 1).

Preparation of the long wave fluorescence linker (Alexa-AC)

An excess amount of AC-OH (5) (666 μmol) and DMAP (66 μmol) were dissolved in DCM and stirred in a lightproof vial purged with N_2 gas. Then, Alexa Fluor 647 carboxylic acid (6), succinimidyl ester (1 μmol) in DMSO was added dropwise, and the mixture was stirred for 32 h at room temperature. After the reaction, the product was neutralized by adding diluted acetic acid. This reaction mixture was extracted with DCM, dried over magnesium sulfate, and evaporated to yield an oily product. The product was purified by silica gel open column chromatography and obtained Alexa-AC (7) (Scheme 1).

Preparation of the nanoparticles

PEG-4AC was prepared as described in our previous report.[16] Then we mixed the solution of 100 μL of 200 mg mL^{-1} PEG-4AC, 100 μL of 100 mg mL^{-1} fluorescent linker (Alexa-AC or PEG-Flu-3AC), 50 μL of 2 mg mL^{-1} physically encapsulated molecule (ferritin or trypsin or Dex-Flu or Dex-Mn), 25 μL of 0.1 M APS, and 25 μL of 0.1 M TEMED in 1 M Tris/HCl buffer in that order and then stirring the mixture for 20 min. After the reaction, the mixture was filtrated by Vivaspin 6–300 K (Sartorius, Germany) at 4000 rpm for 15 min at 4 °C.

Stability analysis of the dispersed nanoparticles

The nanoparticles were dispersed in the mice serum and stored at 37 °C for 12 h. Then the dispersed solution was filtrate by Vivaspin 6–300 K. Then supernatant and filtrate fractions were analyzed by means of dynamic light scattering (DLS) machine (Delsa™ Nano, Beckman Coulter, USA).

TEM observation

Transmission electron microscopy (TEM) images were obtained with an H-7000 electron microscope (Hitachi, Tokyo, Japan) operating at 75 kV. Copper grids (400 mesh) were coated first with a thin film of collodion and then with carbon. The nanoparticle dispersion (1 μL) was placed on the coated copper grids. The stained surface was dried at room temperature before observation.

AFM analysis

Atomic force microscopy (AFM) measurements were conducted by using NanoWizard II (JPK Instrument, Berlin, Germany) at

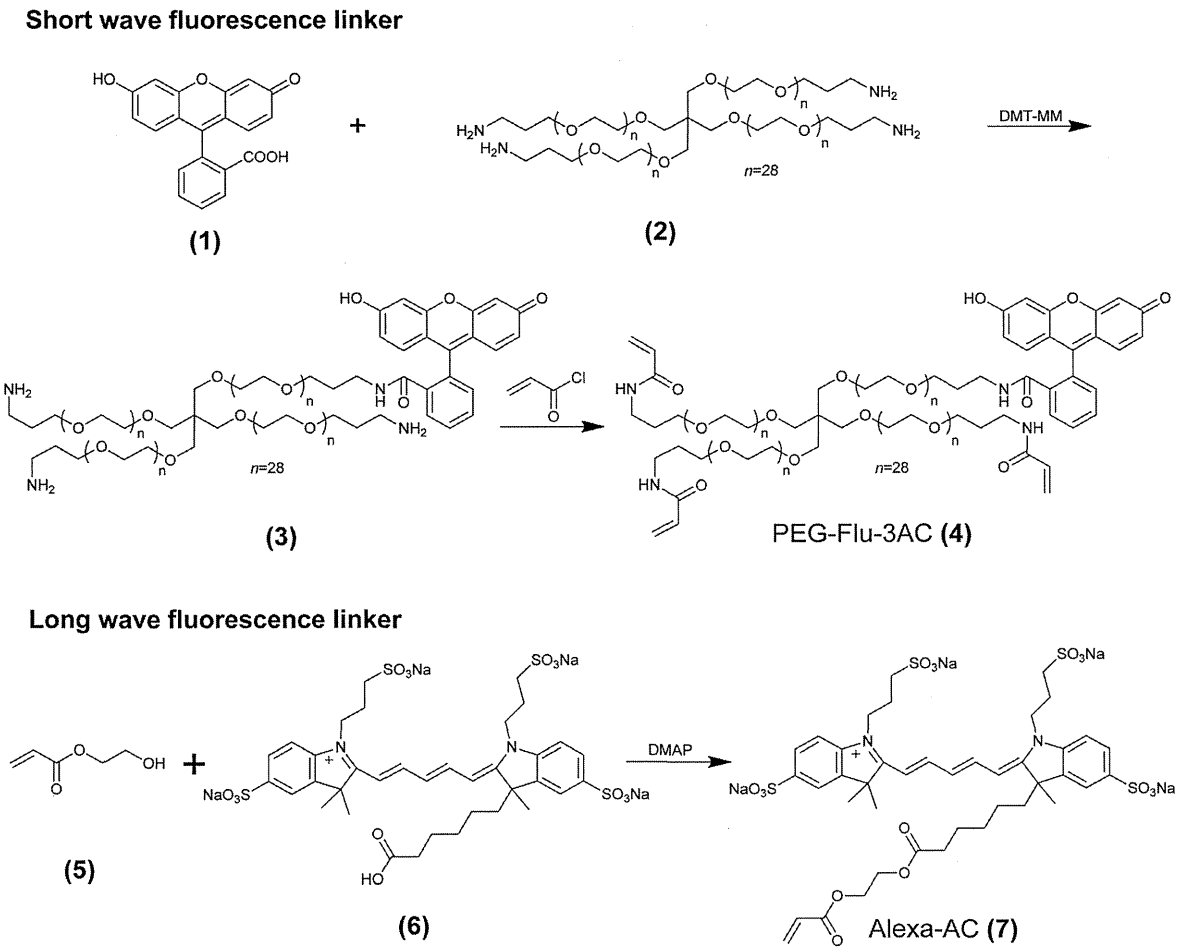

Scheme 1 Preparation procedures for the fluorescence labeled monomers.

room temperature. Images of nanoparticles were obtained in tapping mode using a commercial micro cantilever with a spring constant of 150 N m^{-1} (Olympus Corporation, Tokyo, Japan). AFM images were processed with JPK SPM image processing v.3 software.

In vivo animal study

Female BALB/c nude mice (Japan SLC, Shizuoka, Japan) used for *in vivo* experiments were maintained in accordance with the guidelines of the National Institute of Radiological Sciences (NIRS), and all experiments were reviewed and approved by the institute's committee for care and use of laboratory animals. Colon 26 murine cancer cells (RIKEN BioResource Center, Tsukuba, Japan) were cultured in Dulbecco's modified Eagle's medium (D5796, Sigma-Aldrich, St Louis, MO) supplemented with 10% fetal bovine serum, and incubated in a humidified atmosphere of 5% CO_2 in air at 37 °C. After suspension in phosphate-buffered saline, the cells were subcutaneously inoculated (1.0×10^6 cells/50 μL) into the left flank of the mice. When the tumor mass grew to 5–7 mm in average diameter about 10 days after inoculation, the tumor-bearing mice were used for the following *in vivo* experiments.

In vivo MR imaging of the nanoparticles

Magnetic resonance imaging (MRI) measurements were performed on a 7.0 Tesla horizontal magnet (Kobelco and Jastec, Tokyo, Japan) interfaced to a Bruker Avance I console (Bruker BioSpin, Etlingen, Germany) and controlled with ParaVision 4.0.1 (Bruker BioSpin).

The animal (BALB/c mice) were anesthetized using isoflurane 2.0% and held in a body cradle (Rapid Biomedical, Rimpar, Germany) in the prone position. Rectal temperature was continuously monitored and automatically controlled at 36.5 ± 0.5 °C using a nonmagnetic temperature probe (FOT-M and FTI-10, FISO Technology, Olching, Germany) and an electric temperature controller (E5CN, Omron, Kyoto, Japan) during measurements.

The tail vein was catheterized using a polyethylene tube (PE-10, Becton-Dickinson, Franklin Lakes, NJ) for nanoparticle injection. The mouse was then placed in a proton volume radiofrequency coil (35 mm inner-diameter, Bruker BioSpin) for transmission and reception previously warmed using a body temperature controller (Rapid Biomedical). The resonator units, including the mouse, were placed in the center of the magnet bore. Nanoparticle containing dextran-Mn was intravenously

